

Department of Engineering Physics and Mathematics  
Laboratory of Biomedical Engineering  
Helsinki University of Technology  
Espoo, Finland

# Construction of Boundary Element Models in Bioelectromagnetism

Jyrki Lötjönen

Espoo 2000

Department of Engineering Physics and Mathematics  
Laboratory of Biomedical Engineering  
Helsinki University of Technology  
Espoo, Finland

# **Construction of Boundary Element Models in Bioelectromagnetism**

**Jyrki Lötjönen**

Dissertation for the degree of Doctor of Technology to be presented with due permission for public examination and debate in Auditorium F1 at Helsinki University of Technology (Espoo, Finland) on the 27th of April, 2000, at 12 o'clock noon.

Espoo 2000

# Contents

<b>Preface</b>	<b>ii</b>
<b>List of publications</b>	<b>iii</b>
<b>List of symbols</b>	<b>iv</b>
<b>1 Introduction</b>	<b>1</b>
<b>2 Bioelectromagnetism</b>	<b>3</b>
2.1 Forward problem . . . . .	3
2.2 Source modeling . . . . .	3
2.3 Numerical solution . . . . .	4
2.4 Inverse problem . . . . .	5
2.5 Volume conductor modeling . . . . .	5
<b>3 Anatomic Imaging</b>	<b>7</b>
3.1 Magnetic resonance imaging . . . . .	7
3.2 X-ray imaging . . . . .	8
<b>4 Reconstruction of the 3D Geometry using MR Images</b>	<b>10</b>
4.1 Reconstruction from MR images in this work . . . . .	14
<b>5 Reconstruction of 3D Geometry using X-ray projections</b>	<b>17</b>
5.1 Reconstruction from X-ray projections in this work . . . . .	18
<b>6 Triangulation</b>	<b>22</b>
6.1 Delaunay triangles and tetrahedra . . . . .	22
6.2 3-D Surface Triangulations . . . . .	24
6.3 Triangulation in this work . . . . .	28
<b>7 Registration</b>	<b>32</b>
7.1 Registration of MR images . . . . .	32
7.2 Registration of X-ray images . . . . .	33
<b>8 Boundary element models in practice</b>	<b>34</b>
8.1 Inverse problem studies in the MCG . . . . .	34
8.2 Model properties vs. MCG localization accuracy . . . . .	34
<b>9 Discussion</b>	<b>37</b>
<b>10 Summary of Publications</b>	<b>40</b>

## Preface

This thesis is dedicated to my loving wife Tarja, to our son Markus and to our becoming Mr/Ms X.

The thesis was completed at the Laboratory of Biomedical Engineering, Helsinki University of Technology, and at CREATIS, INSA of Lyon. All magneto- and electrocardiographic measurements were carried out at the BioMag Laboratory at Helsinki University Central Hospital. Magnetic resonance and X-ray images were from the Department of Radiology, Helsinki University Central Hospital, IMIX Oy, Tampere and INSERM, Lyon.

I would like to thank my supervisor, professor Toivo Katila, for his support and for creating excellent conditions for the research. My directors, Dr. Isabelle Magnin and Dr. Tech. Jukka Nenonen, deserve my warmest gratitude for the inspiring research ideas and for the collaboration which was essential for the thesis. In addition, my colleagues at the Laboratory of Biomedical Engineering and at CREATIS deserve my gratitude for many joyful moments and stimulating discussions during the course of the thesis. Finally, I am grateful to my parents and to my Heavenly Father for taking care of me during my whole life.

This work was financially supported by Helsinki University of Technology Foundation, Jenny and Antti Wihuri Foundation, Instrumentarium Science Foundation, Foundation of Technology and Emil Aaltonen Foundation.

Espoo, Mars 2000

Jyrki Lötjönen

## List of publications

This thesis consists of an overview and of the following six publications:

- I J. Lötjönen, P-J. Reissman, I. E. Magnin and T. Katila. Model Extraction from Magnetic Resonance Volume Data Using the Deformable Pyramid. *Medical Image Analysis*, 3(4): 387-406, 1999.
  
- II J. Lötjönen, I. E. Magnin, L. Reinhardt, J. Nenonen and T. Katila. Automatic Reconstruction of 3D Geometry Using 2D Projections and a Geometric Prior Model. *Lecture Notes in Computer Science 1679: Medical Image Computing and Computer-Assisted Intervention, MICCAI'99*, C. Taylor, A. Colchester(Eds.), Springer, 192-201, 1999.
  
- III J. Lötjönen, I. E. Magnin, J. Nenonen and T. Katila. Reconstruction of 3D Geometry Using 2D Profiles and a Geometric Prior Model. *IEEE Transactions on Medical Imaging*, 18(10): 992-1002, 1999.
  
- IV J. Lötjönen, P-J. Reissman, I. E. Magnin, J. Nenonen and T. Katila. A Triangulation Method of an Arbitrary Point Set for Biomagnetic Problems. *IEEE Transactions on Magnetism*, 34(4): 2228-2233, 1998.
  
- V R. Fenici, J. Nenonen, K. Pesola, P. Korhonen, J. Lötjönen, M. Mäkijärvi, L. Toivonen, V-P. Poutanen, P. Keto, T. Katila. Non-fluoroscopic localisation of an amagnetic stimulation catheter by multichannel magnetocardiography. *Pacing Clin. Electrophysiol*, 22: 1210–1220, 1999.
  
- VI K. Pesola, J. Lötjönen, J. Nenonen, I.E. Magnin, K. Lauerma, R. Fenici and T. Katila. The effect of geometry and topology differences in boundary element models on magnetocardiographic localization accuracy. Accepted for publication in *IEEE Transactions on Biomedical Engineering*, 2000.

## List of abbreviations

BEM	boundary element method
CT	computerized tomography
ECG	electrocardiography
EEG	electroencephalography
FEM	finite element method
FFD	free-form deformation
fMRI	functional magnetic resonance imaging
MCG	magnetocardiography
MEG	magnetoencephalography
MR	magnetic resonance
PCA	principal component analysis
PDM	point distribution model
PET	positron emission tomography
RMS	root mean square
SPET	single photon emission tomography
SQUID	superconducting quantum interference device
2-D	two-dimensional
3-D	three-dimensional
4-D	four-dimensional

# 1 Introduction

Electric currents are essential to many biological processes, such as the information transfer in the brain and peripheral nerves, or the activation of the heart. Several diseases are related to problems in the bioelectric activity. The epilepsy, for example, originates from electric discharges in the brain. Concerning cardiac problems, ventricular pre-excitation associated with the Wolff-Parkinson-White syndrome results from an accessory pathway between the atria and the ventricles, while ventricular tachycardia is often caused by myocardial infarction or different cardiomyopathies. Noninvasively obtained information of the sites of such bioelectric problems is often essential for successful treatment of the diseases. For example, noninvasive localizations can improve the result and shorten the time needed in invasive catheter ablation operations in arrhythmia treatment [82].

Multisensor electro- and magnetoencephalographic (EEG and MEG) as well as electro- and magnetocardiographic (ECG and MCG) recordings have been proved useful in noninvasively extracting information on bioelectric excitation [54, 55, 84]. Bioelectromagnetic measurements can be used to investigate normal electric processes, such as spontaneous or evoked brain activation, as well as to study diseases related to electric problems in the body. The measurements provide information which is very difficult to obtain otherwise. Positron emission tomography (PET), single photon emission tomography (SPET) and functional magnetic resonance imaging (fMRI) produce spatially detailed functional information of metabolic processes. Since electric activity and changes in metabolism are often related, these modalities and bioelectromagnetic recordings can measure common activity. Transient and rarely occurring processes, in milliseconds time resolution, can be detected by bioelectromagnetic measurements only. On the other hand, other modalities, such as fMRI, may provide more accurate spatial resolution.

Since the body affects, i.e. filters, the electromagnetic signals measured outside of the body, the anatomy of the patient has to be taken into account, when excitation sites are localized by solving the inverse problem. Boundary element method (BEM) is a widely adopted technique, where the body is modeled as an inhomogeneous volume conductor presented by surfaces, such as scalp, skull and brain in encephalic applications, or thorax, lungs and heart surfaces in cardiac applications. The anatomy of the patient has to be individually modeled, if accurate high-quality inverse solutions are desired.

Modern medical imaging modalities, such as magnetic resonance (MR) imaging and computerized tomography (CT), provide detailed three-dimensional (3-D) anatomic information. MR imaging has established its position as a standard method to retrieve anatomic information for bioelectromagnetic modeling. However, MR images can not be always obtained for bioelectromagnetic inverse studies. In that case, modalities such as conventional X-ray imaging, which is usually easily available and non-expensive, can be used.

The methodology to construct individualized boundary element models for bioelectromagnetic inverse problems is described in this thesis. The process consists of three main steps: 1) reconstruction of the 3-D geometry using either MR or X-ray images, 2) triangulation of the reconstructed geometry, and 3) the registration of the model with the bioelectromagnetic measurement system. This thesis focus on cardiac problems, but the modeling of the head is also addressed. Although the aspects related to bioelectromagnetic problems are emphasized, the methods developed in this thesis, such as segmentation and triangulation, can be applied more generally in various applications.

This thesis is organized as follows. In Chapter 2, different approaches to incorporate patient specific anatomic information for bioelectromagnetic inverse problems are discussed. The imaging modalities and the protocols used are described in Chapter 3. The reconstruction of the 3-D geometry using MR and X-ray images is represented in Chapters 4 and 5. Chapter 6 discusses the triangulation problems, while Chapter 7 describes different solutions for registration. The results of the patient specific boundary element models in practice are shown in Chapter 8. Finally, Chapters 9 and 10 present the discussion and the summary of the methods.



## 2 Bioelectromagnetism

In the following, the forward and inverse problems in bioelectromagnetism are described briefly for the background. The physical and physiological basics of bioelectromagnetic phenomena are not treated here; the reader is suggested to see textbooks (e.g. [104, 105]) and review articles (e.g. [55]).

### 2.1 Forward problem

In bioelectromagnetic modeling, a usual assumption is that the body is considered as a piecewise homogenous volume conductor consisting of  $M$  objects. Each object has a constant conductivity  $\sigma_k$ ,  $k = 1, \dots, M$ . For example, in cardiac applications typical conductivity values are  $\sigma_1 = 0.2 \text{ S/m}$ ,  $\sigma_2 = \sigma_3 = 0.05 \text{ S/m}$  and  $\sigma_4 = \sigma_5 = 0.6 \text{ S/m}$  for thorax, lungs and ventricles, respectively ( $M = 5$ ). The surface  $S_k$  bounds the object  $k$ . The magnetic field due to internal current sources can then be computed from [83]

$$\mathbf{B}(\mathbf{r}) = \mathbf{B}_\infty(\mathbf{r}) - \frac{\mu_o}{4\pi} \sum_{k=1}^M (\sigma'_k - \sigma''_k) \int_{S_k} \phi_{S_k} \mathbf{dS}_k \times \frac{(\mathbf{r} - \mathbf{r}')}{|\mathbf{r} - \mathbf{r}'|^3} \quad (1)$$

where the electric potential  $\phi$  on the surface  $S_l$ ,  $l = 1, \dots, M$ , is obtained from the integral equation [83]

$$(\sigma'_l + \sigma''_l) \phi_{S_l}(\mathbf{r}) = 2\sigma_s \phi_\infty(\mathbf{r}) - \frac{1}{2\pi} \sum_{k=1}^M (\sigma'_k - \sigma''_k) \int_{S_k} \phi_{S_k} \mathbf{dS}_k \cdot \frac{(\mathbf{r} - \mathbf{r}')}{|\mathbf{r} - \mathbf{r}'|^3}. \quad (2)$$

The conductivities inside and outside of the surface  $S_i$  are  $\sigma'_i$  and  $\sigma''_i$ ,  $i = k, l$  respectively. The vector  $\mathbf{r}$  is the position where the field or potential is computed,  $\mathbf{r}'$  represents the points on the object surfaces, and  $\mathbf{dS}_k$  is a surface element oriented along the outward normal of the surface. The conductivity at point  $\mathbf{r}$  on the surface  $S_l$  is referred as  $\sigma_s$  and defined as the average of the conductivities  $\sigma'_l$  and  $\sigma''_l$ . The terms  $\mathbf{B}_\infty(\mathbf{r})$  and  $\phi_\infty(\mathbf{r})$  are the magnetic field and electric potential produced by the current sources in an infinite homogeneous volume conductor.

### 2.2 Source modeling

Since the bioelectromagnetic inverse problem is not uniquely solvable, the actual current sources are replaced by equivalent sources, such as a current dipole, multipole expansions or distributed current sources [55]. In cardiac applications, a uniform double layer approach is also applied [115]. The following description is based on an equivalent current dipole. A dipole is a good approximation of a source distribution which is concentrated to a spatially small area, such as an accessory pathway in the Wolff-Parkinson-White-syndrome.

The magnetic field and electric potential generated in an unbounded volume conductor by a current dipole  $\mathbf{p}$  at the position  $\mathbf{r}''$  are, respectively,

$$\mathbf{B}_\infty(\mathbf{r}) = \frac{\mu_o}{4\pi} \frac{\mathbf{p}(\mathbf{r}'') \times (\mathbf{r} - \mathbf{r}'')}{|\mathbf{r} - \mathbf{r}''|^3} \quad \text{and} \quad \phi_\infty(\mathbf{r}) = \frac{1}{4\pi\sigma_s} \frac{\mathbf{p}(\mathbf{r}'') \cdot (\mathbf{r} - \mathbf{r}'')}{|\mathbf{r} - \mathbf{r}''|^3}. \quad (3)$$

### 2.3 Numerical solution

In our case, the boundary element method is used to solve numerically Eqs. 1 and 2. In the following, we assume a constant potential over each triangle. The triangle  $i$  of the surface  $k$  is represented by  $\Delta_i^k$ . The number of triangles on the surface  $S_k$  is  $n_k$ , and the total number of triangles  $N$ . The discretized version of Eq. 2 can then be written as

$$\phi^l = g^l + \sum_{k=1}^M \omega^{lk} \phi^k \quad (4)$$

where the  $n_l \times 1$  vectors  $\phi^l$  and  $g^l$  consists of  $\phi_j^l$  and  $g_j^l = 2\sigma_s \phi_{\infty,j}^l / (\sigma_l' + \sigma_l'')$ , respectively, at the triangle  $\Delta_j^l$ , and  $\omega^{lk}$  is an  $n_l \times n_k$  matrix

$$\omega_{ji}^{lk} = \frac{\sigma_k' - \sigma_k''}{\sigma_l' + \sigma_l''} \Omega_{ij}. \quad (5)$$

Here  $\Omega_{ij}$  is the solid angle (divided by  $2\pi$ ) subtended by the triangle  $\Delta_i^k$  at the centroid of the triangle  $\Delta_j^l$ . Eq. 4 can be written also in matrix form

$$G = (I - \Omega)\Phi, \quad (6)$$

where  $G$  and  $\Phi$  are  $N \times 1$  vectors containing the  $g_j$  and  $\phi_j$  at each triangle,  $I$  is an identity matrix and  $\Omega$  is an  $N \times N$  matrix consisting of solid angles. Without going to details,  $\Omega$  needs to be deflated in order to be invertible. The vector  $\Phi$  can be computed after a matrix inversion.

The magnetic field can also be expressed using a matrix equation as

$$B = B_\infty + A\Phi. \quad (7)$$

If the magnetic field has been measured in  $P$  positions,  $B$  is a  $P \times 1$  vector containing the magnetic field values at the corresponding points as well as  $B_\infty$  using infinite medium. The vector  $A\Phi$  is a discretized version of the surface integral in Eq. 1. The matrix  $A$  consists of the terms  $a_i \mathbf{n}_i \times (\mathbf{r} - \mathbf{c}_i) / |\mathbf{r} - \mathbf{c}_i|^3$ , where  $a_i$  is the surface area,  $\mathbf{n}_i$  the orientation of the surface normal and  $\mathbf{c}_i$  the centroid of the triangle  $\Delta_i^k$ .

In practice, the use of linear or quadratic base functions [35] has shown to improve the accuracy of BEM calculations. In these cases, the treatment above becomes slightly different. In addition, the dimension of matrices  $\Omega$  and  $A$  becomes smaller ( $\propto$  number of nodes).

## 2.4 Inverse problem

In the restricted inverse problem, the aim is to characterize the bioelectric current sources by finding the parameters of an equivalent generator. Thus, for a current dipole the localization result can be obtained by computing the field for it and comparing the result to the measured field. The dipole parameters (position and moment) are varied and the process is iterated until the residual between the computed and measured fields is minimized. It is worth noting that if the geometry of the model does not change, the matrix  $\mathbf{\Omega}$  needs to be computed only once.

Bioelectromagnetic inverse studies pose difficult and numerically challenging problems. Several different solutions and optimization approaches have been proposed. Since these are not the topics of this work, we only give references for more detailed descriptions, see, e.g. [31, 54, 55, 60, 83, 84, 91, 104, 105, 115]. Recent applications of the inverse studies with focal and distributed sources at Laboratory of Biomedical Engineering in Helsinki University of Technology have been presented in [85].

## 2.5 Volume conductor modeling

In the simplest form, the body as a volume conductor is modeled as a semi-infinite space or a sphere for which an analog solution can be found. Realistically shaped, but non-individualized models have also been widely applied. In those cases, different combinations of the organs have been used, such as homogeneous thorax, thorax with lungs, or thorax with lungs and ventricles in cardiac applications. However, the most accurate results can usually be achieved using individualized models. The requirements for geometric accuracy of the boundary element models, when compared with the MCG localization accuracy, are discussed in Chapter 8. At present, thorax, lungs and epicardium are often modeled in ECG or MCG and scalp, skull and brain in EEG or MEG. In the boundary element models, the brain is represented by a smooth envelope surface. However, the knowledge about the location and orientation of highly convoluted cortex can be utilized to improve the MEG estimate of current sources [94].

The computation and the inversion of the solid angle matrix may become a time-consuming process for very dense triangulations. In practice, a few hundred triangles per surface is typically used in ECG or MCG calculations yielding a computation time of about 30-60 seconds with a standard UNIX workstation. In brain applications, the surfaces up to a few thousands of triangles are used. In theory, the higher the number of triangles the better localization results can be achieved. For numerically stable solutions, it is advantageous to compose the triangles as equilateral as possible. Moreover, triangulations where the size of triangles is smallest near the heart, are often preferred because the electromagnetic gradients show

there largest spatial variations. However, many research groups seem to use contour<sup>1</sup>-based triangulation methods, in which the size of the triangles is difficult to control. Sometimes, it may also be desirable to set triangle points on electrode locations of a multichannel ECG recording. Moreover, the triangulations used for bioelectromagnetic inverse problems have to be isosurfaces, i.e. each edge of a triangle is shared between two neighboring triangles.

Solutions to the model construction, in the context of bioelectromagnetic problems, are not widely reported. In [59], a set of contour points are digitized from each slice of an MR volume using a mouse-driven software. Thereafter, the surface representation is formed by using surface harmonics. Ziolkowski and Brauer segment MR volumes by thresholding, followed by contour tracking. A set of points is chosen from the contours, which are triangulated using a simple contour-based method. The surfaces are represented by a parametric Fourier representation. Yvert *et al.* [124] generate manually contours for one image over two. The triangulation is accomplished using a contour-based method where the problem of branching is also taken into account. Discussions with colleagues from various research groups have indicated that if individualized models are used in bioelectromagnetic problems, they are built more or less manually and the process is often laborious.

The objective of this thesis was to develop methods and software, which constructs boundary element models as automatically and fast as possible. However, the produced models need to follow the restrictions characteristic for bioelectromagnetic inverse problems, such as the number of triangles and their size distribution is pre-defined, the triangles are as equilateral as possible and the surfaces are isosurfaces.

---

<sup>1</sup>A contour is a non-overlapping connected point set on a plane.

### 3 Anatomic Imaging

Various imaging modalities, such as conventional X-ray imaging, ultrasound imaging, X-ray computed tomography (CT), and MR imaging, can be used to acquire anatomic information of patients [1]. Because of low cost, conventional X-ray imaging and ultrasound imaging, providing usually 2-D images, are widely utilized in hospitals and clinics. At present, modern imaging techniques, such as CT and MR imaging, provide spatially detailed 3-D anatomic data, or even 4-D data including time as one more degree of freedom. Since the modalities are based on different physical phenomena, the images provide complementary information. For example CT, based on X-rays, detects bone structures well while MR imaging, based on nuclear magnetic resonance, is supremely suitable for soft-tissue studies.

Several imaging modalities could be used to reconstruct patient specific boundary element models. As mentioned above, MR imaging is widely used for bioelectromagnetic modeling. However, CT images would fit far better, especially in encephalographic studies because the segmentation of the scalp, the skull and the brain envelope is substantially easier from CT than from MR data. However, the extra radiation dose caused by CT, despite the advantages attained in segmentation, usually excludes this modality.

MR imaging is a relatively expensive and time-consuming technique. Moreover, the imaging devices in hospitals are usually reserved for routine examinations and MR imaging can be difficult to arrange within a few hours or even a couple of days for patients suffering from acute cardiac problems. Therefore, it is not always possible to get an MR volume for each subject for bioelectromagnetic inverse studies. However, two orthogonal X-ray projections are usually taken from each patient in the clinical routine before ECG or MCG studies. For these reasons, a method to reconstruct patient specific boundary element models from X-ray projections was developed in this thesis.

#### 3.1 Magnetic resonance imaging

The MR data employed in this work were acquired with a Siemens Magnetom Vision 1.5 T system at the Department of Radiology in Helsinki University Central Hospital. Several imaging sequences have been used, such as a T1-weighted turbo-flash sequence, with the pixel sizes from 1.3 to 2.0 mm and the slice thickness of 10.0 mm. The sequences used have not yet been especially optimized for bioelectromagnetic modeling studies. Usually two data volumes were generated: a transaxial static ECG-gated thorax volume, consisting of slices from the neck down to the pelvis, and a short-axis cardiac cine volume consisting of slices from the valve level down to the apex. The transaxial set contains about 40 slices whereas the cine set consists of 5 – 10 slices at various cardiac phases. Slices from transaxial and short-axis volumes are visualized in Figs. 1a and b.

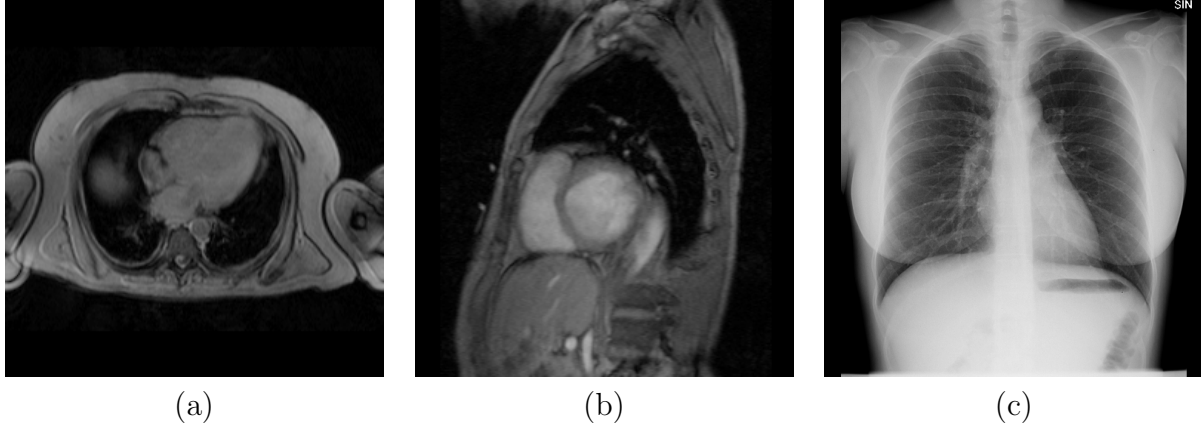


Fig. 1: (a) A transaxial MR image of the thorax. (b) A short-axis MR image of the heart. (c) A frontal X-ray view of the thorax taken from a different patient.

### 3.2 X-ray imaging

The X-ray imaging protocol for individualized bioelectromagnetic thorax modeling has not been established in this work because of practical problems and time limitations given for this thesis. A system to digitize X-ray films or to grab an image from a monitor should be accomplished. Moreover, the inverse problem computations using the ECG or MCG data pose some specific restrictions to the X-ray imaging. First, patients are in the supine position when the ECG or MCG measurements are made while they are usually standing during the conventional thorax imaging. Therefore, the shape and the position of the anatomic objects built from the conventional thorax images differ significantly from the geometry during the ECG or MCG measurements. The way this problem can be solved depends on the features of the imaging device. Second, the images should be ECG-gated, because otherwise the geometry of the heart in the model does not correspond to the end of diastole (QRS), usually investigated in the inverse ECG or MCG studies.

Thus far, the feasibility of X-ray images (Fig. 1c) in the 3-D reconstruction has been tested by simulations. The method developed in this work has been applied to a few conventional thorax X-ray images. Even though the X-ray imaging protocol for the ECG or MCG studies has not yet been established, different ideas are discussed and proposed in this thesis.

The calibration of X-ray projections is necessary in order to retrieve complementary 3-D information from the images. In other words, a relation between each pixel of each 2-D digital X-ray projection and a 3-D coordinate system is established. The two-plane method is an accurate and elegant way to calibrate images [19, 51]. It determines the equations of the 3-D lines corresponding to the X-rays that projected the pixels.

Since the whole reconstruction process, related to the ECG or MCG inverse problem, should be kept as light as possible by minimizing extra efforts needed, the two-plane calibration method can not be applied in our clinical practice. Therefore, a simpler but less

accurate calibration method is proposed.

In this thesis only two X-ray projections are used. The projections are assumed to be orthogonal frontal and side views of thorax. Moreover, the distance of the X-ray source from the film is assumed to be known as well as the distance of the closest point of the patient to the film. The corresponding distances for thorax images in the clinical routine are about 180 cm and about 3 cm respectively. Alternatively, as done in publication V, the relation between the two projections can be determined by defining the distance of an external marker visible in the both images to the film, instead of using the distance of the patient to the film. The accuracy needed to define the distances and the significance of the absolute distance values are discussed below.

## 4 Reconstruction of the 3D Geometry using MR Images

Here, the reconstruction of the 3-D geometry using an MR volume means the segmentation of the images. Since the extraction of shape knowledge by manual segmentation is a long and tedious process, a great number of methods, even in the biomedical field, has been developed to help a user to segment the objects of interests from images [1]. Still, there are no generally applicable, robust and fully automated methods, which would provide the solution within a reasonable time.

Several different approaches, such as region growing and fuzzy clustering, can be used to segment MR images. In medical imaging, the incorporation of knowledge about the shape and the position of anatomic objects is, however, often essential. The images of human organs, containing complex edge structures and lacking some anatomic borders, are sometimes difficult to interpret even for a specialist. Moreover, several other factors, such as noise, partial volume effects and MR field inhomogeneity, may complicate the segmentation. Therefore, the methods based on deformable models are widely used in medical image segmentation and motion tracking [80, 100]. Since a deformable model is based on assumptions of the final result, such as smooth continuous surface, it can partially overcome the problem due to incomplete input data.

The methods based on deformable models can be classified in several ways, as described in [71, 80]. A simple classification is not straightforward because the properties of the methods vary greatly. In this work, deformable models are roughly divided into two groups, methods without and with *a priori* shape knowledge. In other words, the methods with *a priori* shape knowledge are designed to segment objects having similarities to a shape template, whereas the other methods can be applied more generally.

### Deformable models without *a priori* shape knowledge

A physics-based deformable model, also referred to as a snake or an active contour model, is a widely adopted approach, first proposed by Kass *et al.* [64]. The position of the snake is described by a parametric function  $\mathbf{v}(s) = (x(s), y(s))$ ,  $s \in [0, 1]$ . It is deformed by minimizing energy consisting of physics-based internal and external constraint forces, and forces derived from the image to be segmented:

$$E(v) = \int_0^1 (\omega_1(s) \left| \frac{\partial \mathbf{v}}{\partial s} \right| + \omega_2(s) \left| \frac{\partial^2 \mathbf{v}}{\partial s^2} \right|) ds + \int_0^1 P(\mathbf{v}(s)) ds + \int_0^1 E_{ext} ds, \quad (8)$$

where the first integral depicts the internal energy of the snake due to stretching and bending respectively. The functions  $\omega_1(s)$  and  $\omega_2(s)$  give a balance between the physical properties of the model as well as between the physical properties and the other forces. The scalar field  $P(v)$  represent image forces, which are usually defined from image features such as the local



image intensity or gradient. The external constraints are included in the last integral, e.g. a user specified repulsion force at a fixed position. The energy minimum is found numerically by solving the Euler-Lagrange equation.

If the initialization of the snake is far from the desired result, the model may deform to an incorrect local minimum, known as an initialization problem of deformable models. Therefore, modifications have been reported, such as using the balloon force inflating or deflating the model across local minima [27], and applying dynamic programming to find the global energy minimum [48]. The snakes are often initialized by manually drawing a contour or, if 3-D volume data are segmented, using the segmentation result of the previous slice as an initialization. Extensions to real 3-D snakes have also been proposed [25, 34].

Kass *et al.* [64] improve the robustness using a scale-base approach, where the image is low-pass filtered before computing the image forces represented by gradients. The filtering affects in two ways: the effect of small features, e.g. noise, is reduced, and the snakes are attracted from longer distances toward salient edges. A widely adopted multi-resolution approach [7] computes sequentially the scale-base representation and decreases the image resolution by sampling. In addition to the advantages attained using the scale-base approach, the produced pyramid representation reduces the computational complexity of the deformation. In the low resolution images, the size of the image is remarkably decreased providing smaller search-space. Moreover, the pixel-based changes of the deformable model affect large changes in the millimeter scale, extending the attraction field of the image edges. The attraction field can be extended even more by a distance transformation [14], which defines the shortest distance from each pixel to the closest binary edge point in the image. By this approach the range of the attraction field can be basically infinite. Improvements to this approach, such as the gradient vector flow [123], have been reported. A *global-to-local* approach is also widely applied to improve the robustness of the segmentation. It means that gradually more degrees of freedom, often at higher frequencies, are added to the deformable model, i.e. a kind of shape memory is directly included in the deformation process.

Because of local deformations, the conventional snake methods appear to be well suited to shape reconstruction, but they do not fit well to object recognition. The aim of object recognition is to describe the deformations with relatively few parameters. Therefore, methods such as finite element methods (FEM), which is a standard engineering technique, have been developed to parameterize the deformations. A parameterization can be obtained from the eigenvectors of the FEM model corresponding to the object [89, 90]. The eigenvectors are referred to as the free vibration or deformation modes of the 3-D object. Another method is to combine global and local representations. Superquadrics can be used to describe the global shape of the object, whereas the object is locally deformed using the FEM basis functions [52, 109]. Alike method, without using physics-based approach and the FEM, combines superquadrics and free-form deformations (FFD) [9]. In the FFD, a model is positioned in-

side of a regular grid and the model is deformed according to the grid point displacements using linear or spline interpolation [97].

As mentioned above, an initialized model, reasonably close to the desired shape, should be provided for the snake-based methods. Moreover, the snake-based methods do not easily recover shapes containing high frequency components, such as protrusions. A level-set approach, categorized as implicit snakes in [71], has been designed to overcome these problems [76]. The method is based on the idea of propagating wave fronts with curvature-dependent speeds. The method is relatively independent of the initialization and can produce protrusions, such as in a human vessel trees, and changes in topology of the model. Alternatively, a method based on a dynamic triangulated model using Newtonian dynamics and adapting its topology and geometry according to input data can be applied [69]. The deformation is controlled by internal constraints, such as the surface curvature and the distance between the nodes in the triangulation, and external constraints, such as forces defined by the intensities of the input data. A somewhat similar method, using adaptive triangulation without ability to change the topology has also been reported [81].

Alternatively, highly convoluted objects, such as the human cortical surface, are frequently segmented from MR images using hybrid methods by applying several image processing operations [5, 32, 122]. The initial surface or a pre-segmentation is usually extracted by using different image processing techniques, such as local intensity based segmentation methods and morphological operations. The final surface is generated using deformable models.

### **Deformable models with *a priori* shape knowledge**

*A priori* shape knowledge, depicted often by a template, represents the typical shape of the object to be reconstructed. If a shape template is provided, the initialization problem of the conventional snake-based methods is, at least partly, overcome and the segmentation process becomes more robust. Moreover, since the initial shape is close to the desired shape, interactive delineation is not necessarily needed. When the template-based methods are used, the problems of segmentation and registration are equivalent. This chapter concentrates on elastic transformations in the context of segmentation, whereas Chapter 7 discusses rigid registration problems.

The geometrically simplest templates are cylinders [86, 110], superquadrics [11] and hyperquadrics [68] or collections of these simple entities. However, these objects do not usually describe the shape of anatomic objects well enough.

In probabilistic deformable models, the shape of the object is represented by a weighted sum of orthogonal functions, such as Fourier basis-functions, where the probability distributions for the weights, i.e. the parameters, are known [102, 103]. The distributions are determined from a training set. The mean of the distributions defines the initial model, and

the deformation follows the deviation of the distribution around the mean. An objective function to be maximized during the deformation is the sum of two terms indicating the probability of the parameters and the degree of correspondence between the model and the image.

Using probabilistic models, the ability to represent different topologies is limited and a high number of harmonics are needed to model highly convoluted objects. Statistical models are not necessarily subject to this problem; even multiple complex objects can be modeled simultaneously. The Point Distribution Model (PDM), proposed by Cootes *et al.* [30], defines the mean model and its deformation modes consistent with a training set by statistical computations. The model consists of a point set. The mean model is computed by defining the point-to-point correspondence between the different models in the training set and calculating the average for the points. The principal component analysis (PCA) is applied to the point distributions around the mean shape. The eigenvectors of the covariance matrix are defined by the differences of the training set models from the mean model, and they compose the deformation modes of the mean model. The deformation is accomplished iteratively by defining the magnitudes for the deformation modes, which move the model toward the strongest image edges. Instead of using the PDM, the model can be represented by Fourier basis-functions and the deformation modes of the training set can be defined by performing the PCA to the Fourier coefficients [107]. A major problem of statistical models is that the building of a representative training set can be laborious, if the point-to-point correspondence definition can not be automated.

Boundary template models, represented by a contour(s) in 2-D or a surface(s) in 3-D, are similar to statistical shape models, except that the model is not necessary a mean in statistical sense and it is not deformed using statistically defined modes. The boundary templates can be deformed using methods similar to the snakes considering, for example, material stiffness and bending; the difference is that the initialization is pre-defined. McInerney and Kikinis [79] use physics-based approach with FFD to deform a template consisting of surfaces. Non-physics-based approaches are also utilized. Jain *et al.* [61] position a template on a virtual rubber sheet and deform the sheet by orthogonal trigonometric functions of different frequencies. The objective function is defined by the probabilities attached to the weights of the functions, as in [102, 103], and the match of the template with the image. The template used by Lelieveldt *et al.* [71] is a geometric and topologic model representing thorax, lungs, epicardium, ventricles and liver. The organs are modelled using multiple hyperquadric surfaces. The model is matched to the boundaries in the image by varying the scale and the pose of the hyperquadrics. Sandor and Leahy [94] segment the cortical surface using a hybrid method by matching a labeled template with a pre-segmented MR-volume. The labels describe the locations of sulci. The boundary templates are also applied to surface matching, where the template is not matched with the noisy boundaries in the image but

with another surface. For example, two cortical surfaces can be matched based on curvature and fine cortical features [33]. In [108], two surfaces are matched using octree-splines (a kind of FFD) and regulating the size and the change of the displacement vectors. Geometric prior knowledge can also be exploited during the deformation requiring, for example, that the template boundary agrees with the image edges not only in position, but also in the tangent direction [61].

A volumetric template is an extension of the boundary templates. The volumetric template is a volume data set, where each voxel contains a vector consisting of real and symbolic information, such as an anatomic label and gray-scale information from an MR volume. Volumetric templates can be constructed by segmenting, possibly manually, the organs of interest from a representative data volume. The volumetric templates are matched with the patient data by maximizing a correlation measure. The physics-based approaches [7, 21] as well as more heuristic methods, such as FFD [28], can be used.

#### 4.1 Reconstruction from MR images in this work

The segmentation of thorax, lungs, epicardium and ventricles could be solved in several different ways. We first tested segmentation methods based on region growing and snakes [73]. The process was semi-automatic and took about 20-30 minutes to segment one data volume. The segmentation was obviously the most time-consuming part of the whole modeling process.

Another segmentation method, based on the boundary templates, is described in detail in Publication I. The method combines and extends the methods referred in the previous sections. The template is a geometric and topologic model consisting of triangulated surfaces (Figs. 2a and b). The prior model is deformed using FFD (Fig. 2c). The model is matched to input data by moving the points of the deformation grid so that it minimizes the function

$$E_{total} = E_{data} + \gamma E_{model}, \quad (9)$$

where the energy term  $E_{data}$  represents the matching error between the prior model and the partial edges in the input volume, and  $E_{model}$  is an energy component restricting the deformation of the prior model. The balance between the two energy components is set by the parameter  $\gamma$ .

A binary representation of edges is extracted by thresholding either the original gray-scale image or the image produced using standard edge detection methods, such as the Canny-Deriche method [17, 37]. As mentioned above, geometric prior knowledge can be exploited requiring that the boundaries of a given orientation in the model have to match similarly oriented edges in the volume data. This was accomplished by constructing six volume images, which contain only the edges oriented parallel or antiparallel to x-, y- and

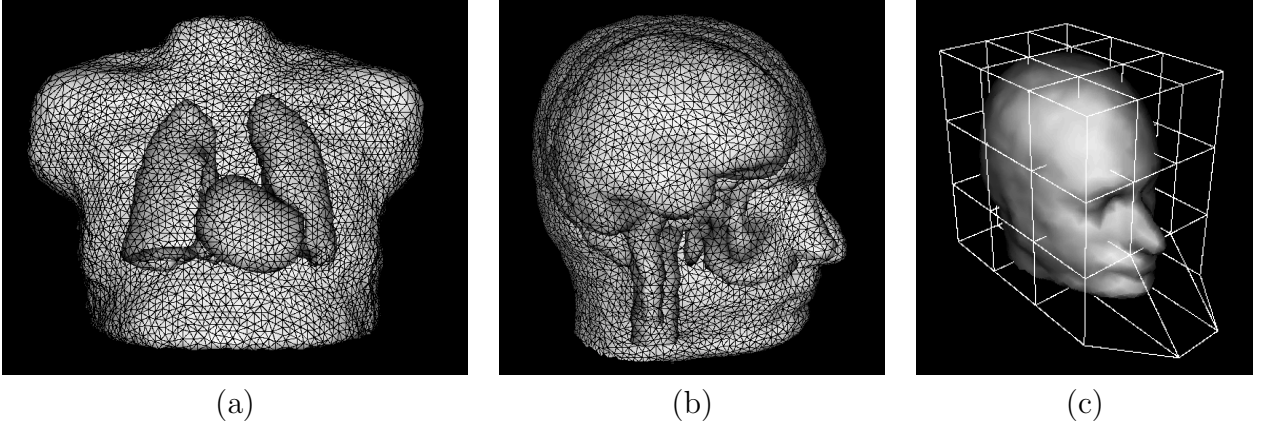


Fig. 2: The prior models of (a) thorax with 9669 nodes and (b) head with 11604 nodes. (c) The prior model inside a  $4 \times 4 \times 4$  deformation grid, in which two grid points have been displaced. (Source: Publication I)

z-coordinate axes. In practice, if the angle between the edge normal and the coordinate axis orientation, related to one of the six volume, is less than  $90^\circ$ , the edge voxel is added to the corresponding volume. The distance transformation [14] is computed for all six volumes. The energy term  $E_{data}$  in Eq. 9 is computed as

$$E_{data} = \frac{1}{N_{nd}} \sum_{l=1}^{N_{nd}} f_i(x_l, y_l, z_l), \quad (10)$$

where

$$f_i : \max\{\mathbf{n}_{mr,i} \cdot \mathbf{n}_{nd,l}\}, \quad i \in \{1, \dots, 6\}. \quad (11)$$

Here, the vector  $\mathbf{n}_{mr,i}$  is the mean orientation of the edges in the distance map  $f_i$ , and the vector  $\mathbf{n}_{nd,l}$  is the surface normal of the model at node  $l$ .

Different regularization terms  $E_{model}$  (Eq. 9) were tested: the displacement of the grid points were minimized, the change in the surface normals as well as in the curvature of the surface were regulated and spring forces were added between the prior model nodes. In many cases, all methods produced good results. In practice, the energy term based on the surface normals is preferred because of its robustness. The energy  $E_{model}$  related to the surface normals is computed as

$$E_{model} = \frac{1}{N_{tr}} \sum_{l=1}^{N_{tr}} (1.0 - \mathbf{n}_l \cdot \mathbf{n}_l^*), \quad (12)$$

where  $N_{tr}$  is the total number of triangles in the model and  $\mathbf{n}_l$  and  $\mathbf{n}_l^*$  are the deformed and the original directions of the normal of the triangle  $l$ , respectively. The normalization factor  $1/N_{tr}$  sets the energy component independent of the number of triangles in the model.

The multi-resolution as well as *global-to-local* approaches were applied. Here, multi-resolution means that the resolution of the volume data is reduced while decreasing the number of nodes in the model simultaneously. The *global-to-local* approach is accomplished as follows. First, the model is coarsely matched with the data. Then, the energy  $E_{total}$  was minimized using a  $3 \times 3 \times 3$  deformation grid. When the minimum was found, the number of grid points is gradually increased. All grid points are moved sequentially toward the minimum using a conjugate gradient method. The process is iterated with a given grid size until the energy does not change more than a user-specified limit. All surfaces are matched simultaneously.

### Examples

So far, the method has been utilized to segment about 40 patient MR volumes of the thorax. Several MR volumes have also been segmented using our head and heart models. The algorithm produces good results, with few interactive corrections. The validation of the result has been accomplished by visual inspection. For 3-D interactive corrections, a software has been developed.

Examples of segmentation results, without interactive corrections, for thorax and head are shown in Fig. 3. As can be noticed, the edges are noisy and many partial edges exist. However, the topological and geometrical prior model overcomes the problem and the overall result is globally good. Because a geometric prior model is used, usually the grid sizes  $9 \times 9 \times 9$  or  $11 \times 11 \times 11$  are enough to obtain a good match between the model and the data. The method is also fast. A typical run time of the program is about 1 minute for thorax, head and heart volumes of the size  $128 \times 128 \times 100$  (SUN Ultra10 workstation).

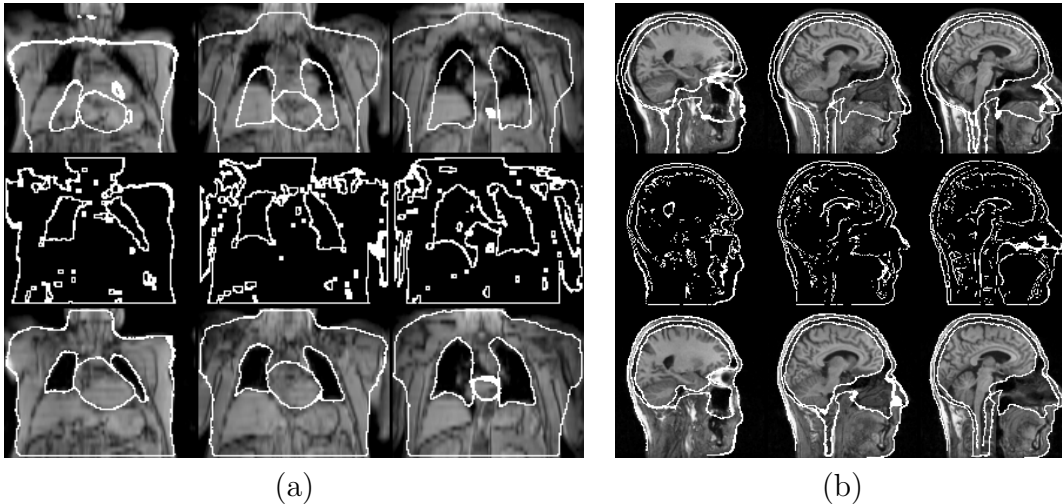


Fig. 3: Segmentation of (a) thorax, a coronal view, and (b) head, a sagittal view. The top row shows the model superimposed onto the data after coarse matching. The middle row represents the edges extracted by an edge detection algorithm. The bottom row shows the final result. (Source: Publication I)

## 5 Reconstruction of 3D Geometry using X-ray projections

An accurate reconstruction of 3-D gray-scale information, for example in CT, is usually based on the use of a high number of projections. If only few projections are used, some *a priori* knowledge can be added to improve the result. For example, Pietikäinen [92] reconstructs knots utilizing three X-ray projections and a priori knowledge of the typical shape and distribution of the knots in logs. However, the methods using few projections are often based only on the reconstruction of the geometry and/or the topology of the objects of interest.

Several approaches have been proposed to extract 3-D tree-like shapes, such as coronary arteries, from biplane angiograms [47, 106, 112, 117]. These methods mainly concentrate on the reconstruction of the topology of the object. The geometry of the object is not emphasized, because arteries and veins can be considered, in general, as pipe-like shapes.

The 3-D reconstruction problem from few projections has not been widely studied and only few references exist. One of the first works concerning the reconstruction of a 3-D object from silhouettes was proposed by Martin and Aggarwal [77]. They produced polygonal 3-D objects by back-projecting the silhouettes. Caponetti and Fanelli [18] presented a method to extract 3-D geometry of bones from two orthogonal projections. The initial estimation of the 3-D bone structure, produced by back-projected profile points, was refined by B-spline interpolation.

In general, the detailed 3-D reconstruction of the geometry is not possible using only information extracted from few projection images. Therefore, methods using *a priori* knowledge are needed. Terzopoulos *et al.* [110] proposed a method to recover the 3-D shape from the 2-D profiles of an object using a deformable tube coupled to a deformable spine. The deformation was controlled by physically based internal and external forces. Bardinet *et al.* [9] presented a method to match a parametric deformable model to unstructured 3-D data. First, they matched a superquadric model to a given point set. Second, the generated superquadric model was deformed locally using FFD. Because of the parametric model and regularization, the method can be used to model sparse data, such as a set of points extracted from few ultrasound images taken from different directions. However, although the methods proposed by Terzopoulos *et al.* and Bardinet *et al.* yield smooth surface between the sparsely distributed points, the geometry produced does not necessarily correspond to the reality.

Methods using *a priori* knowledge of the geometric shapes of the objects of interest overcome, at least partly, the problem. The more sparse data is used, the more evident are the advantages of the geometric model. Fleute and Lavallée [44] proposed recently a method to reconstruct the 3-D geometry of the femur using a few orthogonal X-ray images.

They applied the PDM [30] to build a geometric prior model representing mean shapes and containing the typical deformation modes in statistical sense. Thereafter, they deformed the model non-rigidly, according to the rays back-projected from the contour points of the projections taken from a patient.

## 5.1 Reconstruction from X-ray projections in this work

### Segmentation of X-ray images

The contours of the objects of interest have to be segmented before reconstruction. A review of segmentation methods for X-ray images is not presented in this work. The segmentation of X-ray images is discussed, e.g., in [12, 49].

The segmentation method proposed in publication II is based on publication I. The most important difference is the definition of the prior model. Compared with MR images, edges are smoother and more difficult to define in X-ray projections. Distance maps, calculated from binarized edges in MR data and used to attract the prior model surfaces in 3-D or contours in 2-D, can not be easily utilized with X-ray images. Therefore, the prior model is an X-ray image similar to the one to be segmented but taken from a different patient (Fig. 4). The prior model is a representative of typical anatomy. The model is matched with the input image using FFD in such a way that the similarity between the two images is maximized. Since the model is pre-segmented, the segmentation of the input image can be produced automatically. Even very weak edges can be correctly localized because they now appear at equivalent positions both in the input image and in the prior model. However, the contrast and brightness differences in the original X-ray images cause problems. They can be at least partly overcome by matching gradient images calculated using the Canny-operator [17] (Fig. 4). The matching error  $E_{data}$  between the model and data gradients is defined by

$$E_{data} = \frac{1}{N_G} \sum_{i=1}^{N_G} \|\mathbf{G}^D(x_i, y_i) - \mathbf{G}_i^M\|^2, \quad (13)$$

where the function  $\mathbf{G}^D(x, y)$  is the gradient image of input data,  $\mathbf{G}_i^M$  is a gradient vector from the gradient image of the prior model, and  $N_G$  is the total number of these vectors. The function  $\mathbf{G}^D(x, y)$  is evaluated at the position  $(x_i, y_i)$  of the gradient  $\mathbf{G}_i^M$ . The symbol  $\|\cdot\|$  denotes vector norm. It is worth noting that the function  $\mathbf{G}^D(x, y)$  and the gradients  $\mathbf{G}_i^M$  remain constant during deformation. Only the position  $(x_i, y_i)$  of each model gradient is varying.

The minimization of  $E_{data}$  does not guarantee that the prior knowledge of the model shape is preserved. Therefore, the deformation must be regularized. The changes in the normal directions of the contour points, defined by the pre-segmented model, are used.

The highest grid size of  $10 \times 10$  is usually large enough for thorax images. After reaching



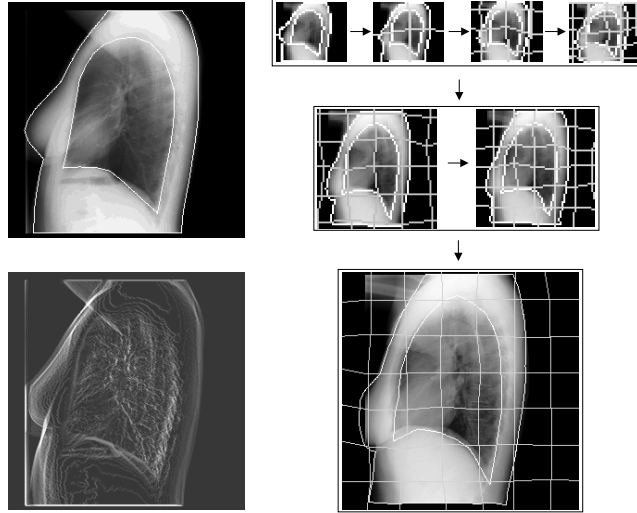


Fig. 4: *On the left: The prior model (up) and the corresponding gradient image (bottom), showing only the position and the magnitude of the gradient. On the right: the multi-resolution and the global-to-local approaches. The deformed prior model contour and a deformation grid are superimposed onto the input data. (Source: Publication II)*

the highest grid size the resolution level of the volume data is changed, i.e. the multi-resolution approach has been adopted. The multi-resolution and global-to-local approaches are demonstrated by vertical and horizontal arrows in Fig. 4.

Since a geometric prior model is used in the 3-D reconstruction, the complete segmentation of the contours is not necessary. Therefore, alternatively only a set of landmark points can be manually selected in couple of minutes, instead of segmenting the whole contour.

## Reconstruction

Conventionally, a prior model is elastically matched in 3-D to the fan beams produced by back-projected contour points in different projections [43, 44, 51, 70]. In principle, the trace of the back-projected contour point forms a 3-D line, which touches tangentially the 3-D surface. The assumption is correct if the projection process and therefore the projection image were binary. Unfortunately, when gray-scale X-ray images are segmented and the contour points are back-projected, the produced 3-D lines are generally not precisely tangential to the corresponding 3-D object. There are at least two reasons for this:

- Neither a human nor a computer vision process locates the contour points in the same way as the binary projection.
- Segmentation errors can not be avoided.

If the 3-D model is deformed towards the 3-D lines, the first problem imposes a systematic error to the deformation process. Therefore, a different approach was chosen in this work.

The prior model used is similar to the model used in the MR segmentation, consisting of the triangulated surfaces of the thorax and the lungs. Virtual projections are produced

from the prior model by simulating real X-ray imaging conditions. The pose, shape and size should correspond approximately to those of the patient during the X-ray imaging. Lavallée and Szeliski [70] proposed a method of registering a 3-D model with the fan beams produced by the contour points. However, there are several aspects to be taken into account before using the method. First, Lavallée and Szeliski applied the method for intra-patient registration. Second, the method assumes that the profiles are produced by the convex-hull of the prior model, which is not the case with lungs. Third, the problem of binary vs. non-binary projections is present. Moreover, since the lung profile contains information on both lungs in the side view, they cannot be registered separately. For these reasons, we used only a manual version of their method.

In addition to the real patient images, the virtual X-ray images are segmented. The contours of the virtual X-ray images are thereafter elastically matched with the contours of the patient producing 2-D displacement vectors for each contour point of the virtual projections. If the segmentation method described above is used, the matching is produced automatically. Moreover, the matching is also straightforward if the manually selected landmarks are used.

Next, the 2-D displacement vectors are back-projected onto the positions of the 3-D prior model surface which produced the corresponding contour points. The linked list of the back-projected positions are referred as apparent contours [51]. The back-projected displacement vectors form a spatially sparse displacement vector field.

Several methods could be used to compute the deformation vector for an arbitrary surface point of the prior model. Fleute and Lavallée [44] used statistically defined typical deformation modes to elastically match the model according to the fan beams. Instead of using the fan beams, this method can be also applied to utilize displacement vectors in some specific locations. In our work, we applied FFD with the global-to-local approach. The change in the normal directions of the prior model surface points was controlled. Moreover, linear interpolation using geodesic distances on the surface can be used to compute the displacement vectors. Linear interpolation is faster than shape-based interpolation. However, in general it does not aim to preserve the shape of the original prior model during the deformation.

## Examples

Two segmented thorax X-ray images are shown in Figs. 5a and b. The global accuracy of the results is good. The comparison of the models reconstructed from two X-ray projections and from MR images, for example, contains always registration errors, and the separation between reconstruction and registration errors is difficult. Therefore, the accuracy of the reconstruction method was verified by simulation. Virtual X-ray projections were produced from 15 segmented MR volumes, 3-D models were reconstructed from these projections and the final models were compared with the original MR volumes. Figs. 5c and d show the deformed models superimposed onto the corresponding MR volume in the best and in the

worst cases. The average errors, i.e. the distance of the deformed model nodes to the MR volume surface, in the 15 cases were for thorax, left lung and right lung 1.21, 1.20 and 1.26 voxels, respectively, corresponding to a real distance of about 5 mm.

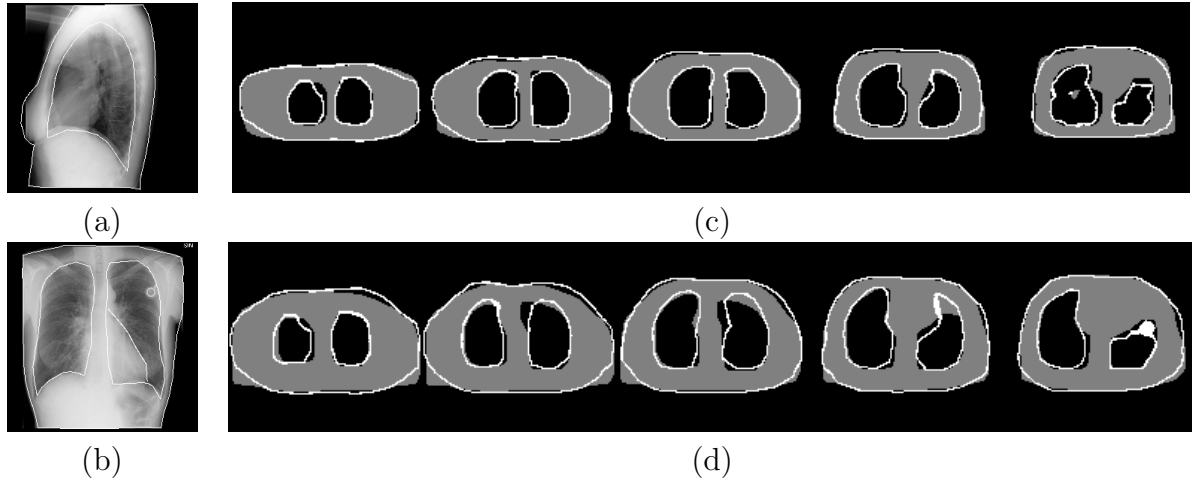


Fig. 5: A segmentation result of thorax images, (a) side view, (b) frontal view. A deformed model superimposed onto transaxial MR images (c) in the best case and (d) in the worst case.

The reconstruction process can be simplified and speeded up if the following assumptions can be made: 1) the imaging geometry is known and fixed, 2) the prior model represents the patient well, i.e. the pose, shape and size of the prior model correspond approximately to the geometry of the patient, and 3) the shape of the contours is not very sensitive to small coarse registration errors. The assumptions were tested by comparing the result produced after coarse registration using fan beams, with the result produced when only fixed virtual projections were used but the centers of mass of each object were registered. Using the centers of mass the average error was only 0.05 voxels (0.2 mm) higher than using the fan beams. In practice, the difference is so small that the assumptions can be regarded as valid in this case.

The effects of errors in imaging geometry were also studied. The position of the X-ray source both in the direction and orthogonal to the beam, was varied by 3 cm. The error increased maximally by about 0.1 voxels. Therefore, small errors in the definition of the X-ray imaging geometry do not change the result significantly. The distance of the X-ray source and the closest point of the patient from the film were assumed to be 180 cm and 3 cm respectively. The absolute values of distances are not of great importance for the reconstruction method but the values should be known in order to create virtual X-ray images of the model using the correct imaging geometry. Obviously, if the distance of the X-ray source from the film is reduced, the positions of the back-projected vectors from different projections become closer to each other spatially. In that case, the complementary 3-D information produced by different projections is decreased.

## 6 Triangulation

Surface representations are needed in a variety of disciplines, such as computer graphics, geographic information systems, and finite-element engineering problems. The geometric models representing the surfaces of 3-D objects are often described by a set of triangles or parametric functions, as already seen in the previous chapters. The most important reason for the popularity of triangulations is their simple structure: they can be represented by a point set and a list of triangles. Since the structure is simple, different surface parameters and transformations can be calculated easily and fast.

Triangulation, in general, is a widely studied problem [6, 63]. Among triangulation methods, Delaunay triangulation is regarded as a gold-standard. The popularity of Delaunay triangulation is based on the property that the triangles are as well-shaped as possible. This means that the triangles are as equiangular as possible, i.e. the smallest angle of Delaunay triangles has been maximized. This property is preferred in many applications. Although Delaunay triangulation does not produce directly a 3-D surface triangulation, i.e. a boundary element model, but a planar triangulation for a 2-D point set and a tetrahedrization for a 3-D point set, it is the basis for several surface triangulation methods.

### 6.1 Delaunay triangles and tetrahedra

The triangulation of a point set  $p$  in  $n$ -dimensional space  $E^n$  can be defined using the duality between Voronoi and Delaunay diagrams [6]. The Voronoi area  $V_i$  of a point  $p_i$  is

$$V_i = \{P \in E^n \mid \forall j \in [1, m], d(P, p_i) \leq d(P, p_j)\}, \quad (14)$$

where  $m$  is the number of the points in the set and  $d$  is the Euclidean distance between the specified points. In other words, all points  $P$  in  $E^n$  which are closest to point  $p_i$  define the Voronoi area  $V_i$ . Delaunay triangulation is produced when neighboring Voronoi areas are connected by edges. Fig. 6 shows the Voronoi-Delaunay duality. Delaunay triangulation is unique, provided that the points are in general position, i.e. no four points lie on a common plane, and no five points lie on a common sphere.

Delaunay triangulation can also be defined using an alternative method. Given a point set  $p$  in  $n$ -dimensional space  $E^n$ ,  $k$ -simplex is defined as the convex combination of  $k+1$  affinely independent points in  $p$ , i.e. a triangle is a 2-simplex and a tetrahedron is a 3-simplex. In a Delaunay triangulation, a hyper-sphere circumscribed around  $n+1$  points of each simplex contains no other point of the set  $p$ .

The Voronoi-Delaunay duality is not often used in Delaunay triangulation construction but the hyper-sphere and equilaterality criteria are preferred. A numerous amount of 3-D triangulation methods has been developed. Delaunay triangulation methods can be classified as follows [24]:

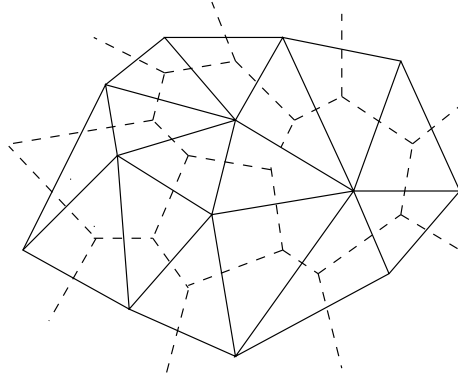


Fig. 6: *The Voronoi-Delaunay-duality. The Voronoi-diagram is represented by dashed lines and the corresponding Delaunay triangulation by solid lines.*

- *Local Improvement (LI)* [29]. An arbitrary triangulation is generated. Thereafter, edges of simplices are flipped (or the term “swapped” is also used) according to the equilaterality criterion.
- *Incremental Insertion (II)* [16, 50, 99, 113, 118, 119, 121, 126]. A simplex containing the convex hull<sup>2</sup> is created. The points  $p$  are inserted sequentially in such a way that the simplex, containing the new point, and the simplices around it are deleted and the hole produced is retriangulated using the hyper-sphere or the equilaterality criteria. This method is also called *online-method*.
- *Incremental Construction (IC)* [24]. The algorithm creates a simplex using the points  $p$  and satisfying the hyper-sphere criterion, i.e. a simplex which belongs to the final Delaunay triangulation. More simplices are added sequentially around the original simplex until all points  $p$  are triangulated.
- *Higher Dimensional Embedding (HDE)* [8]. The point set  $p$  in  $E^n$  is transformed to  $E^{n+1}$  and the convex hull is defined. Delaunay triangulation is obtained by projecting the convex hull back to  $E^n$ .
- *Divide & Conquer (DC)* [24]. The method is based on recursive partition of the point set  $p$  and the local triangulation of these subsets. The final triangulation is formed by merging the local triangulations.

The list of relevant algorithms is endless. Moreover, their ranking is difficult because of different requirements set for the algorithms. If finite-element methods are used instead

---

<sup>2</sup>The convex hull of a point set is the intersection of all half-spaces containing this set [6]. Delaunay triangulation in 3-D generates tetrahedra which are inside the convex hull of an object of interest. Therefore, 3-D Delaunay triangulation produces a surface triangulation for a given point set, but it represents the convex hull of the object. If the object contains concave areas, the surface triangulation does not represent the real surface of the object.

of boundary-element methods in bioelectromagnetic inverse problems, the methods able to produce *constrained* Delaunay triangulations [20] should be preferred. Constrained Delaunay triangulation contains a set of pre-defined edges and is simultaneously as close as possible to Delaunay triangulation. Since Delaunay triangulation produces triangulation inside the convex hull, constrained triangulations are usually necessary, when real, non-convex, objects are modeled. Moreover, if the point set to be triangulated consists of points from several objects, constraints are needed to produce triangulations respecting the interfaces of the objects. The methods [29, 50, 119, 121] mentioned above can generate constrained Delaunay triangulations and are therefore applicable in finite-element modeling.

## 6.2 3-D Surface Triangulations

A categorization of surface triangulation methods is shown in Fig. 7. The input data available and output data required restrict the choice of the triangulation method.

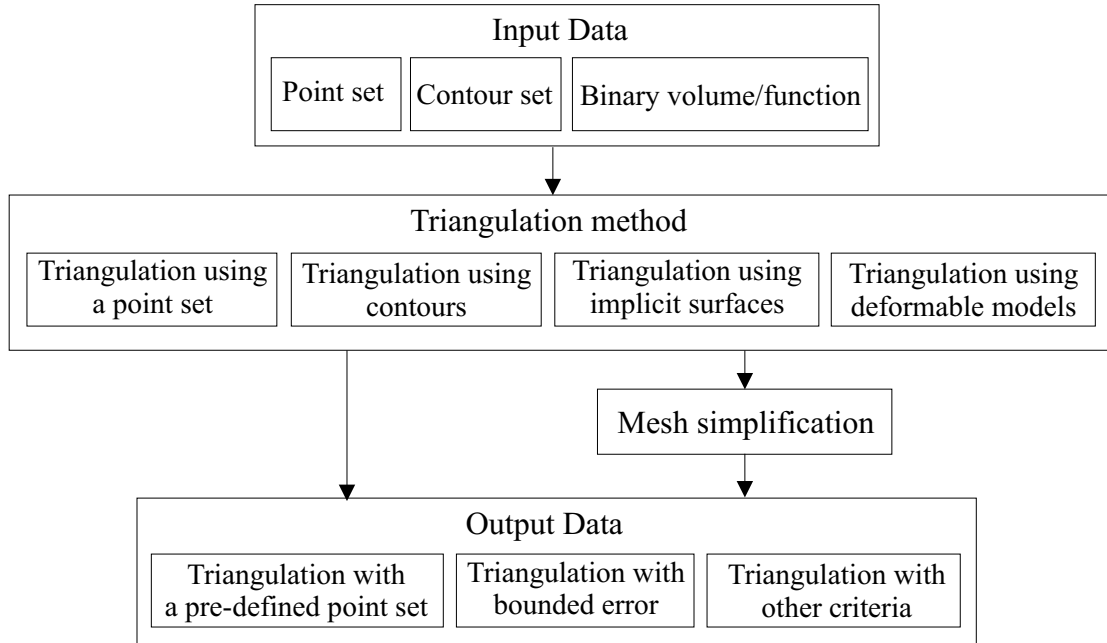


Fig. 7: *Triangulation flow-chart.*

### Input Data

Input data are coarsely classified into three groups, representing data from unorganized to organized: *point set*, *contour set* and *binary volume/function*.

As mentioned above, a contour is a non-overlapping connected point set on a plane. The difference between a point set and a contour set is that a point set is totally unorganized, while the neighbors of the points are known within a contour but not between the contours. The group *binary volume/function* means that complete surface information is available of the object of interest, e.g. described by a mathematical function.

The borders of the input data groups are not always clear. The *binary volume/function* representation can always be transformed to a point or a contour set. However, the reconstruction of volume data from a point or a contour set is not unique, in general. This is a common problem in the signal processing community. As an analog signal is sampled, it can not be accurately reconstructed if the sampling frequency is lower than two times the highest frequency in the analytic signal (the Nyquist law). In other words, if a sparse point set from a highly curved object is available without any *a priori* knowledge of the surface between the points, the topologic and geometric correctness of the result can not be guaranteed. The terms sparse and dense point sets should be related to the complexity of the object and the desired resolution of the reconstruction. The definition of the frequency content of a 3-D surface as well as the definition of a sparse and dense point set are not, however, straightforward.

In medical applications, input data can be generated from several different sources. The modern 3-D medical imaging techniques, such as MR and CT, produce a set of slices. When the slices are segmented, either a set of contours or a binary volume representation are generated. In general, the produced volume representation can not be regarded as complete characterization, since the smallest geometric and topologic details of the object are limited by the voxel size. However, if one can assume that the object does not contain finer details than the voxel size or the details are not interesting for the present application, the representation can be called *binary volume/function*. In many data volumes, the distance between the slices is much larger than the distance between the pixels in the slice, i.e. a slice thickness is large or a gap between slices exists. Although the voxel size can be decreased by interpolation, it is worth noting that no new details can be produced. In addition to images, geometric information can be produced using, for example, a 3-D digitization system, which gives 3-D coordinates for points specified by the user.

## Output Data

Three groups of output data are proposed. First, the group *Triangulation with a pre-defined point set* contains triangulations where the point distribution is defined by the user. Second, the geometric accuracy of the final triangulation instead of the point distribution itself is emphasized in some applications. This is accomplished by bounding the geometric error below a user-defined parameter  $\epsilon$ . This group is denoted by *Triangulation with bounded error*. The third group *Triangulation with other criteria* contains all other results, such as the cases where only the number of triangles is pre-defined.

## Triangulation using a point set

The methods designed to triangulate an unorganized point set can be divided to surface- and volume-based approaches. In surface-based methods, the triangulation problem is solved using heuristic rules basically in 2-D. For instance, the idea of the incremental construction

method can be utilized, i.e. more triangles are added around an existing triangulation sequentially [13]. In volume-based methods, the problem is first transformed entirely to 3-D by computing Delaunay tetrahedrization [3, 13, 39] or a more general 3-D representation [116]. The final surface triangulation is generated by removing tetrahedra or edges of the 3-D representation. However, a Delaunay tetrahedrization does not necessarily contain a simple closed polygon through all surface points. For this reason, the elimination of the tetrahedra can get locked.

### Triangulation using contours

In contour-based methods, a set of contours located on different planes are connected to each other by triangles. In general, the triangulation of contours is easier than the triangulation of an unorganized point set, because the neighborhood relations between the points within a contour are known. Since modern medical imaging techniques, such as MR and CT imaging, produce a stack of 2-D slices of an object of interest, the contour-based methods can be used in several medical applications.

The contour-based methods can be coarsely classified into two categories: heuristic and graph-based methods. In heuristic methods triangles are added one after another using local triangulation rules [10, 22, 41, 46, 67]. The graph-based methods, typically employing dynamic programming, optimize a specific property of the triangulation, for example, the surface area of the triangulation can be minimized [45], the volume of the triangulation maximized [66], or geometrically the most similar parts of the contours are connected [65].

The topology of the object is correctly represented if each level contains only one contour. If the number of contours is higher, it is not self-evident, which contours should be connected with each other. The problem is usually solved by matching a box around the contours and comparing their cross-sections [40, 127]. Haig *et al.* [53] proposed theoretical rules to connect the planes containing several contours. Yet another problem is branching. It means that the connectivity between the contours is not a *one-to-one* mapping, for example, two contours on the level  $k$  are fused to one contour on the level  $k + 1$ . Several solutions exist for the problem [22, 40, 96, 98].

In addition to the topologic problems, the contour-based methods have other restrictions. If the size or the shape of the contours to be connected differs considerably, non-equilateral triangles can not be avoided. Moreover, the methods can be used to triangulate a point set located on parallel slices, i.e. the points can not be arbitrarily distributed. The advantage of the contour-based methods is that they are fast and easy to implement. Therefore, if the final triangulation does not have any restrictions except possibly the number of triangles, and the object of interest is relatively simple, the contour-based methods can be recommended.



### Triangulation using implicit surfaces

In many cases detailed geometric information, i.e. an implicit surface representation<sup>3</sup>, is available. Input data from the group *binary volume/function* is of this type. However, a method to generate a volumic representation for an unorganized point set has also been reported [57]. The methods based on implicit surfaces choose automatically a very dense point set from the surface. The number of triangles can be even millions, which is too high for many applications. Therefore, mesh simplification methods have to be applied.

Lorensen and Cline proposed a widely adopted marching cubes method to generate a detailed triangulation from volume data [72]. A  $2 \times 2 \times 2$  mask is moved over the volume. In each position, a triangulation corresponding the voxel values within the mask is retrieved from a look-up table and fused to the triangulation created at previous positions. Since the length of the triangle edges is about one voxel, i.e. even single voxels are triangulated, the geometry and the topology is accurately described; obviously assuming that sub-voxel details are neither interesting nor desired. In addition to the marching cubes method, other implicit surface approaches exist, too [56].

### Triangulation using deformable models

Segmentation methods based on deformable models were described in the previous chapters. These approaches are not usually regarded as triangulation methods. However, a triangulation can be produced as a by-product in many cases where deformable models are used. If a deformable model consists of triangles, the final deformed model is a triangulation. The points present in the final triangulation are, however, more or less arbitrarily positioned. In the methods based on deformable models, the correct reconstruction of the geometry and topology is emphasized more than triangulation aspects. Obviously, if the number of triangles is high in the result, mesh simplification algorithms can be applied and any output data format can be produced. In most cases, the methods based on deformable models are too complicated, if only triangulation is needed. However, in the case that the input data are a sparse or noisy point set, superior results compared with the other methods can be achieved using a geometric and topologic prior model; a priori knowledge of the geometry between the points is utilized.

### Mesh simplification

Mesh-simplification, also referred to as decimation, methods can be coarsely categorized into two groups: the methods which guarantee that the simplified triangulation approximates the original mesh to within a specified tolerance  $\epsilon$ , and the methods, which generate a triangulation for a pre-defined sparse point set without controlling the approximation error. However, there are also heuristic methods, which belong to neither group [87].

---

<sup>3</sup>Implicit surfaces can be presented using a function  $f = f(\mathbf{x})$ , which gives the shortest distance to a surface. The surface triangulation is defined by polygonalizing the zero set of the function, i.e.  $f(\mathbf{x}) = 0$ .

The methods based on maximum approximation error reduce the number of points usually iteratively until the error level of  $\epsilon$  is reached. In the simplest form, the distance from a candidate vertex to the plane defined by the vertices around the candidate is calculated, then the vertex is removed if this distance is higher than a user-specified limit, and the resulting hole is retriangulated [95]. Methods based on a more global error measure have been also reported [23, 62, 101]. Moreover, several relevant but totally different approaches have been proposed [26, 38, 58, 63].

Besides our work, we are aware of only one other method producing a triangulation for a pre-defined point set [114]. Turk [114] removed points iteratively, as in the methods based on bounded error. He produced first a triangulation for the union of the pre-defined points and the points of the original triangulation, i.e. the triangulation to be simplified. Thereafter, all vertices belonging to the original triangulation were removed iteratively.

### Other triangulation aspects

In some cases constrained triangulations are needed. If triangles are added (or deleted using simplification methods) to an existing triangulation iteratively, the constraints are easier to include than using non-interactive methods, such as Voronoi-Delaunay duality. However, if constraints are not or can not be accomplished during the triangulation, the final triangulation can be post-processed, e.g. by swapping the edges in such a way that the constraints are included in the result.

The triangulation problem of data with boundaries is usually not discussed in the papers referred above. However, most methods can be extended to include data with boundaries. The simplification methods produce always triangulations with boundaries, if the original triangulation contains boundaries.

## 6.3 Triangulation in this work

Typically, bioelectromagnetic inverse calculations impose several restrictions for triangulations, such as equilaterality and the requirement of the small size of the triangles near the heart, as described in Chapter 2. The methods fulfilling the requirements are discussed next.

As mentioned above, Delaunay triangles are as equilateral as possible. However, if the point set is non-uniformly distributed, the triangles may be far from equilateral, although the equilaterality of the triangles has been maximized. Therefore, a sampling method should be chosen to enable equilateral triangles.

### Selection of a point set

Turk [114] proposed an iterative method to produce uniform point distributions. A point set is first distributed randomly over the surface, and then each point is allowed to repel all its neighbors. In addition to the distance between the points, the forces can also depend on

the curvature of the surface or the distance from the user-specified gravity point, as described below.

An alternative non-iterative method is represented in publication IV. Let  $R$  be the edge length of equilateral triangles. The sampling can be accomplished using the following method:

1. Select two arbitrary points from the surface in such a way that the geodesic distance between the points is  $R$  (points 1 and 2 in Fig. 8).
2. Label the area of the surface which is closer than  $R$  from the selected points (gray area in Fig. 8).
3. Choose a point from the border of the labeled area in such a way that the distance to two closest points inside the labeled area is  $R$  (either the point 3 or 4 in Fig. 8). Repeat steps 2 and 3 until the whole surface has been labeled.

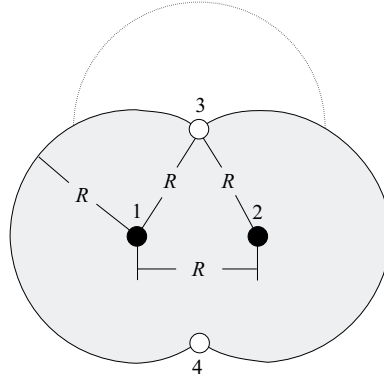


Fig. 8: *Selection of the points for triangulation on a planar surface. (Source: Publication IV)*

If the point set is chosen from a planar surface, the Delaunay triangles will be equilateral. For a general 3-D surface, the equilaterality assumption can not be strictly followed. Although the method does not guarantee a theoretically optimal result, it is fast and gives regular enough results for bioelectromagnetic inverse problem calculations.

The size of triangles can be varied on the surface of the object by defining different values for  $R$  from place to place. For example, if a higher density of triangles is desired, e.g., in the vicinity of the heart, the user defines first a gravity point in the center of the heart. Then,  $R$ -value can be locally computed as

$$R = R_{min} \left( \frac{d}{d_{min}} \right)^f, \quad (15)$$

where  $R_{min}$  corresponds to the smallest desired edge length of the triangle closest to the gravity point(s),  $d$  is the distance from the gravity point(s) to the point of interest on the

surface, and  $d_{min}$  is the shortest distance from the gravity point to the same surface. The exponent  $f$  controls the rate of the change of the parameter  $R$  in function of the distance.

### Triangulation

For connecting the selected points, two triangulation methods are reported in this work: a method utilizing implicit surfaces and mesh-simplification, and a method based on deformable models.

At the beginning, a very dense triangulation, giving a detailed description of the geometry and the topology of the object of interest, is generated for a segmented volume data using a method based on implicit surfaces, such as the marching cubes algorithm. Thereafter, the number of triangles is reduced. A non-iterative simplification method is utilized producing a triangulation for a pre-defined point set. We apply the method described in detail in publication IV. The Voronoi-areas are defined first for the pre-defined points using geodesic distances on the 3-D marching cubes triangulation. The distances are calculated using the edges of the triangles. The final triangulation is generated using the Voronoi-Delaunay-duality.

Alternatively, a method based on deformable models can be applied. If a triangulated boundary template is used during the MR segmentation, the segmentation and the triangulation problems can be solved simultaneously. The method proposed in publication I is used. In addition to the prior model used in the segmentation, one more triangulation is generated satisfying the restrictions given for bioelectromagnetic inverse problems. This model is deformed using the same transformation as was applied for the original prior model. In this case, two different model-based energy components are used: the change in the normal direction of the surface and the energy due to spring forces. The stronger is the impact of the spring force, the closer is the shape of the triangles to the original shape. However, if the string force component is too strong, the geometric accuracy of the segmentation may be poor.

### Examples

Figs. 9a and b show boundary element models of the thorax and the head, respectively, when the method based on mesh simplification was applied. The method can be also used to triangulate more complicated objects, such as the brain in Fig. 9c. The method is fully automatic and fast. The computation time to select a point set, to calculate the marching cubes triangulation and to simplify the mesh takes about 3 seconds using a Sun Ultra10 workstation. The size of volume data was  $128 \times 128 \times 128$ . Since the method is non-iterative, the computation time does not depend, in practice, on the number of triangles in the final mesh. The method is robust: hitherto hundreds of triangulations have been successfully generated.

Fig. 9d shows a triangulation of the thorax when deformable models were utilized. Al-

though the triangles are not Delaunay triangles after deformation, the shape of the triangles is visually satisfactory. The strong point of this method is that no traditional triangulation methods are needed but the segmentation algorithm produces the triangulation as a by-product.

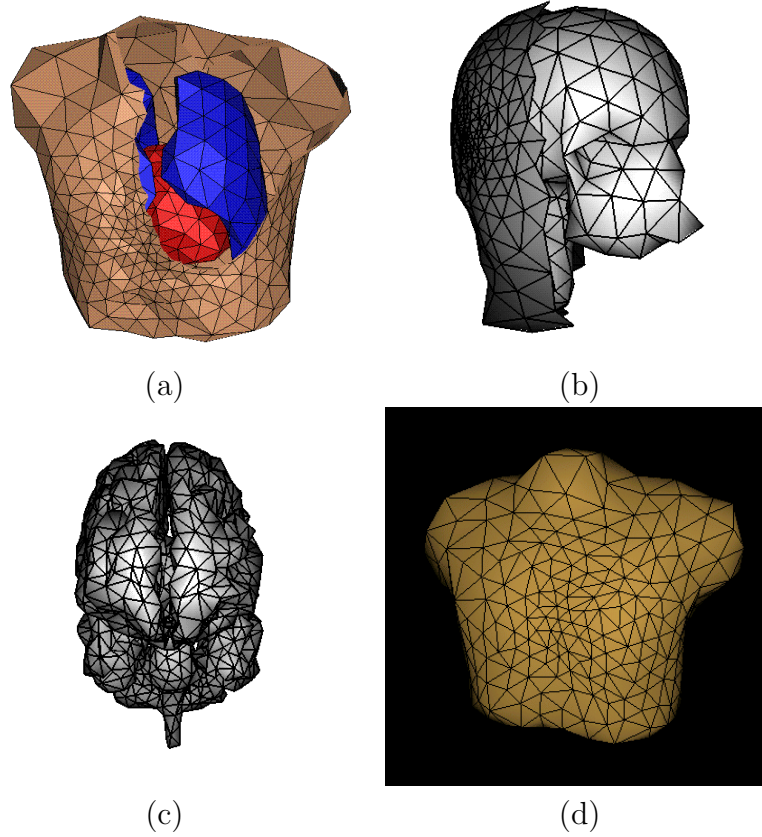


Fig. 9: *Triangulation results using a method based on simplification of the marching cubes triangulation: (a) the triangulation of thorax, lungs and epicardium, (b) the triangulation of scalp ( $R_{min} = 1.5$  and  $f = 1.1$ , Eq. 15) and skull ( $R = 10$ ) and (c) the triangulation of brain ( $R = 5$ ) - frontal view. (d) Triangulation using a deformable model ( $R_{min} = 1.5$  and  $f = 1.0$ ). (Source: Publication IV)*

## 7 Registration

Medical images or data, such as ECG or MCG localization results acquired in the clinical work, are of a complementary nature. Therefore, proper interpretation and comparison of data from different modalities can be accomplished by transforming all data into common spatial alignment, which is also referred to as registration. Since this work does not focus on registration algorithms, a detailed review of different methods is not provided. A good and recent review of registration methods can be found in [75].

The ECG and MCG data used in this work were recorded from patients at the BioMag-laboratory in Helsinki University Central Hospital (HUCH). The problem here is the registration of either the MR or the X-ray coordinate system with the ECG or MCG coordinate system. The registration is needed in order to transform the model constructed from anatomic images to the ECG or MCG coordinate system for inverse problem calculations. In addition, the localization results need to be transformed to a clinically useful presentation, such as to patient anatomy in the real MR or X-ray images. The registration is not straightforward because ECG/MCG measurements do not provide any anatomic landmarks but produce results in the measurement device coordinate system. In the HUCH BioMag laboratory, the position of the measurement dewar with respect to the patient is typically determined by measuring the magnetic field arising from current fed into small marker coils attached to the skin, and by calculating their locations relatively to the sensor array [2]. The locations of the coils are recorded with a 3-D digitization system (3SPACE, Polhemus Inc., Colchester, VT, USA).

The registration algorithms can be coarsely divided to three groups which register: 1) a set of landmark points, such as external markers and anatomic landmarks [4, 78, 93], 2) geometric image features, such as surfaces [15, 36, 42, 88], and 3) image intensity based measures, such as mutual information [74, 120]. Since the relation between the ECG or MCG and an anatomic imaging device coordinate systems can be established using only a point set, recorded by the 3-D digitization system, the registration methods based on image intensities can not be used. Basically two solutions exist: 1) External markers are attached on the skin of the patient, localized by the digitization system and located from anatomic images, and finally, the two point sets are registered; 2) Using the surface-based matching methods, the model produced from anatomic images is registered with a large set of points digitized from the skin of the patient.

### 7.1 Registration of MR images

In this thesis, a method based on external markers was adopted. In our ECG or MCG studies, nine marker locations are used. Five positions are digitized in head-feet direction centered to the sternum and other four in left-right direction, forming a cross-shaped pattern. The

separation between neighboring markers is about 5 cm. The digitized positions are stamped with non-toxic ink, visible only in ultraviolet light. Before MR imaging, external cross-shaped markers, filled with 1mmol/1MnCl<sub>2</sub> fluid, are placed on the stamped positions. The cross-shaped figure of a marker is clearly visible in MR images. The markers are manually localized from MR images using a special software. An automated marker detection software is under development. The nine markers digitized both in the ECG or MCG and MR coordinate system are registered using a non-iterative least-squares method [93]. The transformations discussed here are rigid, i.e. only rotations and translations are concerned.

The RMS-error of the registered external markers is about 6 mm in our patient studies. The absolute value of the error is not high concerning the different sources of error, such as breathing, reattachment of the markers between ECG or MCG and MR measurements, shape changes between the measurements because of flexibility of the shoulders and the skin, and because of different shapes of the measurement beds (ECG or MCG bed is flat, MR bed is concave), and localization accuracy of the markers from MR images. However, in the scope of the ECG or MCG localization accuracy, the registration error is relatively high and should be reduced. A study for further reduction of different error sources is still ongoing.

The use of the surface-based registration methods is attractive because the extra work related to marker positioning is avoided. However, there may exist several other problems. For example, the flexibility of the shoulders may cause problems. On the other hand, if the shoulder area is excluded from the registration, as done in our external marker approach, problems may appear in the head-feet registration, because the shape of the thorax is not far from a cylinder. The applicability of the surface-based registration will be considered in the ongoing error study.

The head in EEG/MEG studies can also be registered using either marker- or surface-based methods. Anatomic landmarks, such as nasion and periauricular points, can be used. The problems related to the elasticity of the object are smaller, because the skull of the human head is a rigid object.

## 7.2 Registration of X-ray images

As mentioned above, an X-ray imaging protocol has not yet been established for our patient studies. However, approaches similar to the MR registration could be used. The external markers containing fluid should be replaced, for example, by a set of small pieces of lead, visible in X-ray images. The basic idea in the X-ray image-based modeling is the simplicity itself. Therefore, the feasibility of the surface-based registration methods should be charted. The registration problem in the head-feet direction could be avoided by incorporating anatomic knowledge, such as the heads of the clavicles close to sternum, visible in X-ray images and possible to identify using the 3-D digitization system.

## 8 Boundary element models in practice

### 8.1 Inverse problem studies in the MCG

MCG studies were performed at the BioMag laboratory in HUCH. The recordings were obtained in a magnetically shielded room (Euroshield Ltd., Eura, Finland) using a 68-channel cardiomagnetometer (Neuromag Ltd., Helsinki, Finland). Besides the MCG signals, it was possible to record simultaneously up to 128 ECG channels.

The construction of patient-specific thorax models for ECG or MCG inverse problems using MR images can be summarized as follows:

1. Interpolate MR volumes, i.e. transaxial whole thorax and short-axis heart, as isotropic.
2. Segment the volumes using the thorax model, including thorax, lungs and epicardium, and the heart model, including epicardium and ventricles, and verify the results using an interactive software.
3. Generate binary volumes from the deformed prior models and triangulate the volumes.
4. Transform the short-axis result to the coordinate system of the transaxial volume using the header information of the volumes.
5. Locate manually external markers from the transaxial volume and transform the boundary element model to the ECG or MCG coordinate system.

Registered and patient-specific boundary element models can be built in 10 – 15 minutes from an MR data volume using the described protocol.

The model construction protocol developed in this work has been successfully applied in several MCG/ECG studies, such as in [91] and in publication V. In the latter work, the localization of an amagnetic catheter and sources of cardiac evoked fields were studied. The amagnetic catheter can be applied in invasive recordings during the MCG aiming at non-fluoroscopic catheter localization in arrhythmia ablations. The localization results are visualized in the triangulation and on MR images in Figs. 10a and b respectively. The localization accuracy obtained in the referred papers was about 1 cm, which is useful for pre-surgical evaluation of arrhythmia patients.

### 8.2 Model properties vs. MCG localization accuracy

The effect of the boundary element model properties to bioelectromagnetic forward and inverse problems have been covered in several papers [31, 60, 111, 125]. To our knowledge, however, a systematic study has not been reported earlier. In publication VI, the effects of various sources of error in boundary element model construction to the dipole localization



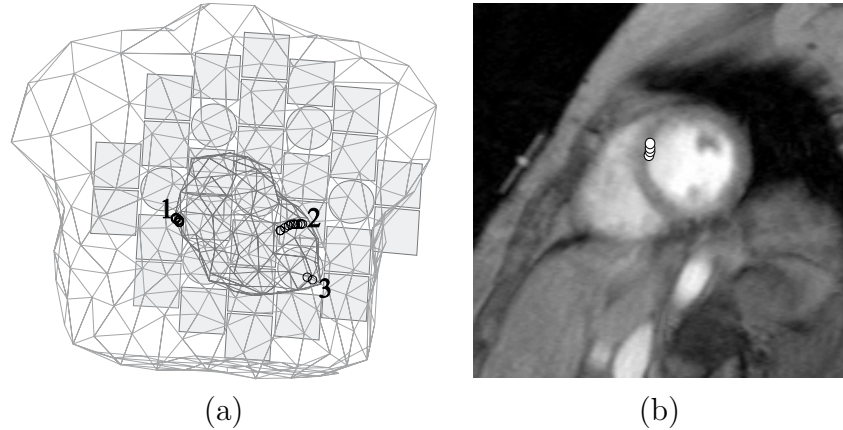


Fig. 10: (a) Frontal view of the boundary element torso model of a patient. The outer thorax boundary is represented by 672 triangles, while the pericardial surface was divided into 182 triangles. Open circles refer to the MCG localization results in sinus rhythm: (1) during initial 20 ms of atrial activation, (2) during initial 20 ms of ventricular depolarization, and (3) during pacing at the stimulus peak and during the reponse 3 ms later. Outlines of measurement sensors are also depicted. (b) MCG localization results of a patient overlaid on short-axis MR images of the heart: Spontaneous ventricular depolarization during initial 10 ms of the QRS complex (2 ms step). (Source: Publication V)

accuracy from multichannel MCG recordings were studied. Simulated and real data from three patients were used. A dipole was localized first with a boundary element model generated using the protocol presented in this work. The result was regarded as a *gold standard*. Thereafter, different properties were altered including the number and the distribution of triangles, the size and shape of the model, registration parameters, and various combinations of the parameters. The dipole was then localized and the result was compared to the gold standard.

The interpretation of the results is not straightforward. However, different guidelines were found and can be summarized as follows:

- Small, even invisible, geometric errors in the model changed the localization result about 5 mm providing an idea of the effect produced by unavoidable errors during the MR model construction.
- On the other hand, non-individualized but realistically shaped models caused only 10 – 15 mm errors.
- The accuracy of the result with X-ray projection-based models were between MR-based and non-individualized model results.
- The results change even several centimeters when inhomogenities are excluded.

and more specifically,

- The model of the thorax should extend at least 20 – 25 cm below the apex of the heart.
- The localization result is highly sensitive to the position of the lungs and ventricles, which should be taken into account when non-individualized models are used.
- The number and the distribution of the triangles is not extremely important in the localization, but non-equilateral triangles may cause even 10 mm errors in some cases.
- The localization result is not especially sensitive to geometric errors nor translation and rotation errors in any specific coordinate direction.

As a conclusion, the difference in the localization accuracy, when the MR-based and non-individualized models are used, is small but remarkable, about 5 – 10 mm. However, it is worth noting that the effect of geometric errors is bipartite. Although the modeling errors did not affect the localization accuracy in the MCG coordinate system, i.e. different errors could compensate each others, the result can be visualized for a clinician into an incorrect place in anatomic images, if the position or the shape of the epicardium and ventricles is wrong. This is especially problem with non-individualized models when no information is available from internal anatomic structures.

## 9 Discussion

A protocol to reconstruct individualized boundary element models from MR or X-ray images for bioelectromagnetic inverse problems has been realized in this thesis. The main focus is in cardiac applications. The construction process can be divided into three main parts: 3-D reconstruction, triangulation, and registration.

Two methods utilizing MR and X-ray images have been developed for the 3-D reconstruction. Both approaches are based on the use of a 3-D prior model in the context of deformable models. When MR images are used, the method has to cope with noisy and complex edge structures in the images. In the case of X-ray images, the method deforms the prior model utilizing highly limited information available from two orthogonal projections. However, the use of a geometric and topologic prior model combined with shape preservation provided a good approach for the given problem.

A major problem with the present imaging modalities is that ECG or MCG recordings and anatomic images are not acquired during the same session. Hence the pose of the patient may differ in separate measurements. The registration error of about 6 mm between the boundary element model and the points defined by the digitization system is an indication of this problem. Bioelectric measurements could be run simultaneously with MR or X-ray imaging by using special arrangements. Anatomic imaging during the biomagnetic recordings is, however, today not possible, because the magnetic sensors (SQUIDS) are very sensitive to magnetic materials near the measurement dewar. However, an approximation could be obtained, if the anatomic information were extracted just before magnetic measurements outside the magnetically shielded room without moving the patient. Easily available and mobile alternative modalities, such as the 3-D digitization system and ultrasound images, could also be used to extract anatomic information. Because of patient movements between the bioelectromagnetic and anatomic recordings, a set of 3-D points digitized from the skin of the patient would be, in practice, the optimal data source for the reconstruction of thorax surface. The segmentation method developed for MR images can be used to reconstruct a boundary element model from digitized points, i.e. a geometric prior model is matched with the point set. Some preliminary tests have been already done by matching a prior model to the points digitized from endocardium during animal examinations. Ultrasound images could be used to reconstruct the 3-D geometry of ventricles. The method developed for X-ray images could be utilized. However, two problems need to be addressed: 1) The position of the ultrasound images related to the heart anatomy should be known in order to select correct cross-sections from the prior model. 2) The relation of the ultrasound images to the anatomy of the patient should be defined in order to position the ventricles correctly compared with the thorax.

A triangulation method was developed with the aim of satisfying the requirements set

by the bioelectromagnetic inverse problem, such as equilaterality and pre-defined density of triangles. A set of points are first distributed onto the surface of the object as uniformly as possible, however, fulfilling the density criterion. Thereafter, the marching cubes triangulation is computed for the object and the triangulation is simplified in such a way that only the pre-defined points stay in the triangulation. The final triangulation is an approximation of the Delaunay triangulation defined as a dual of the geodesically defined Voronoi areas computed for the pre-defined points. However, both MR- and X-ray-based reconstruction methods produce as a result an isosurface containing the appropriate number of triangles, if these properties are satisfied in the original prior model. Moreover, because the global-to-local approach is used, the magnitude of the high-frequency deformations is usually small and therefore the shape of the triangles does not change significantly from the original shape. For these reasons, a separate triangulation method is not necessary, but the transformation defined in the 3-D reconstruction can be applied to a model satisfying the requirements of the bioelectromagnetic inverse problem.

The produced triangulation is finally transformed to the coordinates of the electromagnetic measurement system using rigid registration based on external markers. At present, the registration accuracy of about 6 mm is achieved. However, the value is relatively high compared with about 1 cm localization accuracy requirement for clinical applicability in cardiac studies. Obviously, the registration error can be suppressed by applying elastic registration/deformation after rigid registration. Methods based on free-form deformation or statistical point distribution model could be used. The surface of thorax, after elastic transformation, corresponds to the geometry of the patient during the bioelectromagnetic measurements. However, the problem is that no information is presently available how the lungs and the ventricles should be transformed. Because of lacking information, probably the best choice is to deform these objects simultaneously with the thorax to preserve the relative positions between the objects. The transformation of this kind is easy to produce using free-form deformation. However, it is worth noting that the preservation of the relative positions is not necessarily correct because of elasticity of the body, especially the fat under the skin.

More than fifty boundary element models have been successfully constructed from MR images using the methods developed in this work. The protocol developed is fast and robust. In order to further improve the protocol, an easy-to-use software should be built, where all methods are gathered under one user-interface. In addition, the practical problems related to X-ray imaging should be solved in order to start the model construction for real patient studies.

As mentioned above, the localization accuracy of about 1 cm is useful for pre-surgical evaluation of cardiac arrhythmia patients. In the context of our study, this requirement can be attained with MR- and X-ray-based models. However, in addition to model properties,

other factors affect the localization accuracy, including measurement noise, the source model and the activation site in the heart. Therefore, more accurate model constructions have to be still endeavoured. In the future, the representation of the patient anatomy *during* real bioelectromagnetic measurements must be emphasized; a careful analysis of modeling errors need to be conducted first.

## 10 Summary of Publications

### Publication I

Model Extraction from Magnetic Resonance Volume Data Using the Deformable Pyramid (Med. Image Anal., 3(4), 387-406, 1999)

A geometric and topologic 3-D prior model is deformed using free-form deformation (FFD) toward noisy and incomplete edges in MR images. The robustness of the method is improved by utilizing regularization and the global-to-local approaches. Visually good segmentation results, needing about one minute computation time in a standard UNIX workstation, are achieved when the method is applied to thorax, brain and heart MR volumes of the size  $128 \times 128 \times 100$ .

### Publication II

Automatic Reconstruction of 3D Geometry Using 2D Projections and a Geometric Prior Model (Lecture Notes in Computer Science 1679: Medical Image Computing and Computer-Assisted Intervention, MICCAI'99, C. Taylor, A. Colchester(Eds.), Springer, 192-201, 1999)

The 3-D surfaces of the thorax and the lungs are reconstructed automatically from two orthogonal X-ray projections. A segmentation method based on free-form deformation (FFD) is proposed and a reconstruction method utilizing the segmented contours is shortly described. A heuristic shape-based interpolation method is used in the reconstruction. The volumes of the lungs are also computed and the accuracy of the measure is studied.

### Publication III

Reconstruction of 3D Geometry Using 2D Profiles and a Geometric Prior Model (IEEE Trans. Med. Imag., 18(10), 992-1002, 1999)

The reconstruction of 3-D geometry using two orthogonal X-ray projections is described. Virtual X-ray projections are first computed for a geometric prior model consisting of the surfaces of the thorax and the lungs. Thereafter, the contours of the objects of interest are segmented from real patient images and the virtual X-ray projections, and the contours are matched. The deformation vectors produced are then back-projected onto the original prior model surface. The prior model is deformed using shape-based interpolation using FFD. The reconstruction error of the method is about 1.2 voxels corresponding to about 5 mm for thorax and lungs.

### Publication IV

A Triangulation Method of an Arbitrary Point Set for Biomagnetic Problems (IEEE Trans. Magn., 34(4), 2228-2233, 1998)

A binary data volume is triangulated by utilizing the Voronoi-Delaunay duality. First, a

dense marching cubes triangulation is computed for the binary volume. Second, a point set is chosen conforming to the restrictions set by the bioelectromagnetic inverse problem. Third, the marching cubes triangulation is simplified in such a way that only the points chosen exist in the final triangulation; the simplification is subject to the topology preservation of the original marching cubes triangulation. The simplification is accomplished non-iteratively, i.e. the Voronoi areas are computed for the points chosen using discrete geodesic distances and the final triangulation is generated by connecting the neighboring Voronoi areas. The method is successfully applied to binarized MR volumes of the thorax and the head. The method is robust and computes the result in a few seconds for a volume of the size  $128 \times 128 \times 100$ .

### **Publication V**

Non-fluoroscopic localisation of an amagnetic stimulation catheter by multichannel magnetocardiography (PACE, 22, 1210–1220, 1999)

The accuracy of noninvasive magnetocardiographic localization is studied using an amagnetic stimulation catheter. Both the catheter and paced myocardial evoked responses are localized. Individualized boundary element models are used in the inverse computations. The results are compared to the catheter positions defined in X-ray fluoroscopy images. The mean distance between the position of the tip of the catheter defined from X-ray fluoroscopy and the MCG localization was  $11 \pm 4$  mm.

### **Publication VI**

The effect of geometry and topology differences in boundary element models on magnetocardiographic localization accuracy (Accepted for publication in IEEE Trans. Biomed. Eng., 2000)

The boundary element model properties are systematically varied and the change in the magnetocardiographic (MCG) localization result is monitored. This is accomplished by regarding one model as a gold-standard and detecting the MCG localization difference between the modified and the gold-standard model. About one hundred properties are studied consisting of the geometric accuracy, the number and the shape of the triangles and the rigid registration errors. Several relations were found, such as very small geometric errors change the localization result even 5 mm, relatively large geometric errors do not change the result more than 10 – 15 mm and the localization result is not very sensitive to the number of triangles.

### **Author's contribution**

In publication I, the author continued and extended the work reported in the PhD-thesis of the second author by proposing, for example, different regularization terms, the global-to-local approach, and the oriented distance-maps. He also tested the applicability of the

method to various objects of interest. Moreover, the whole software was implemented and the prior models were constructed by the author. The methodological work concerning the segmentation and reconstruction methods in publications II and III was done by the author. In addition, the author implemented and tested the methods developed. In publication IV, a major part of the algorithm development was accomplished by the author. The author also implemented the method and tested it using several data volumes. The author constructed the individualized boundary element models used in publication V. Moreover, the registration of MCG and MR coordinate systems were at authors response. In publication VI, the first two authors were mainly responsible for the experimental paradigm. The author also designed and constructed the model library. The main part of publications I-IV and about half of publication VI was written by the author.



## References

- [1] R. Acharya and R. P. Menon. *Deformable Models in Medical Image Analysis*, chapter A Review of Biomedical Image Segmentation Techniques, pages 140–161. IEEE Computer Society Press, 1998.
- [2] S. Ahlfors and R. J. Ilmoniemi. Magnetometer position indicator for multichannel meg. In S.J. Williamson, editor, *Advances in Biomagnetism*, pages 693–696. Plenum Press, 1989.
- [3] N. Amenta, M. Bern, and M. Kamvysselis. A new voronoi-based surface reconstruction algorithm. In *Computer Graphics Proceedings, SIGGRAPH*, pages 415–421, 1998.
- [4] K. S. Arun, T. S. Huang, and S. D. Blostein. Least-squares fitting of two 3-d point sets. *IEEE Trans. Pattern Anal. Machine Intell.*, 9(5):698–700, 1987.
- [5] M. S. Atkins and B. T. Mackiewicz. Fully automatic segmentation of the brain in mri. *IEEE Trans. Med. Imag.*, 17(1):98–107, 1998.
- [6] F. Aurenhammer. Voronoi diagrams - a survey of a fundamental geometric data structure. *ACM Computing Surveys*, 23(3):345–405, 1991.
- [7] R. Bajcsy and S. Kovacic. Multiresolution elastic matching. *Computer Vision, Graphics and Image Processing*, 46:1–21, 1989.
- [8] C. B. Barber, D. P. Dobkin, and H. T. Huhdanpaa. The quickhull algorithm for convex hulls. *ACM Trans. on Mathematical Software*, 22:469–483, 1996.
- [9] E. Bardinet, L. D. Cohen, and N. Ayache. A parametric deformable model to fit unstructured 3d data. *CVGIP: Computer Vision and Image Understanding*, 71(1):39–54, 1998.
- [10] C. Barillot, A. Bouliou, G. L. Certen, J. L. Coatrieux, R. Collorec, B. Gibaud, O. Lis, and L. L. Min. Computer graphics in medicine: a survey. *CRC Critical Reviews in Biomedical Engineering*, 15(4):269–306, 1988.
- [11] A. H. Barr. Superquadrics and angle-preserving transformations. *IEEE Computer Graphics and Applications*, 1(1):11–23, 1981.
- [12] G. Behiels, D. Vandermeulen, F. Maes, P. Suetens, and P. Dewaele. Active shape model-based segmentation of digital x-ray images. In C. Taylor and A. Cochester, editors, *Lecture Notes in Computer Science 1679: Medical Image Computing and Computer-Assisted Intervention, MICCAI99*, pages 128–137. Springer, 1999.
- [13] J-D. Boissonnat. Geometric structures for three-dimensional shape representation. *ACM Trans. Graph.*, 3(4):266–286, 1984.
- [14] G. Borgefors. Distance transformation in digital images. *Computer Vision Graphics and Image Processing*, 48:344–371, 1986.
- [15] G. Borgefors. Hierarchical chamfer matching: A parametric edge matching algorithm. *IEEE Trans. Pattern Anal. Machine Intell.*, 10(6):849–865, 1988.
- [16] A. Bowyer. Computing dirichlet tessellations. *The Computer Journal*, 24(2):162–166, 1981.
- [17] J. Canny. A computational approach to edge detection. *IEEE Trans. Pattern Anal. Machine Intell.*, 8(6):679–698, 1986.
- [18] L. Caponetti and A. M. Fanelli. Computer-aided simulation for bone surgery. *IEEE Computer Graphics and Applications*, 13(6):86–91, 1993.
- [19] G. Champlébourg, S. Lavallée, P. Sautot, and P. Cinquin. Accurate calibration of cameras and range imaging sensors: the npbs method. In *IEEE International Conference on Robotics and Automation*, pages 1552–1557, 1992.
- [20] L. P. Chew. Constrained delaunay triangulation. *Algorithmica*, 4(1):97–108, 1989.
- [21] G. E. Christensen, R. D. Rabbitt, and M. I. Miller. 3d brain mapping using a deformable neuroanatomy. *Physics in Medicine and Biology*, 39:609–618, 1994.

- [22] H. N. Christiansen and T. W. Sederberg. Conversion of complex contour line definitions into polygonal element mosaics. *Computer Graphics: A Quartely Report of SIGGRAPH-ACM*, 12:187–192, 1978.
- [23] A. Ciampalini, P. Cignoni, C. Montani, and R. Scopigno. Multiresolution decimation based on global error. *The Visual Computer*, 13(5):228–246, 1997.
- [24] P. Cignoni, C. Montani, and A. Scopigno. Dewall: a fast divide & conquer delaunay triangulation algorithm in ed. *Computer-Aided Desing*, 30(5):921–941, 1998.
- [25] I. Cohen, L. D. Cohen, and N. Ayache. Using deformable surfaces to segment 3-d images and infer differential structures. *CVGIP: Image Understanding*, 56(2):242–263, 1992.
- [26] J. Cohen, A. Varshney, D. Manocha, G. Turk, H. Weber, P. Agarwal, F. Brooks, and W. Wright. Simplification envelopes. *Computer Graphics*, 30:19–26, 1996.
- [27] L. D. Cohen. On active contour models and balloons. *CVGIP: Image Understanding*, 53(2):211–218, 1991.
- [28] D. L. Collins, C-J. Holme, T. M. Peters, and A. C. Evans. Automatic 3-d model-based neuroanatomical segmentation. *Human Brain Mapping*, 3:190–208, 1995.
- [29] P. Conti, M. Toimizawa, and A. Yoshii. Generation of oriented three-dimensional delaunay grids suitable for the control volume integration method. *International Journal for Numerical Methods in Engineering*, 37:3211–3227, 1994.
- [30] T. F. Cootes, C. J. Taylor, D. H. Cooper, and J. Graham. Active shape models - their training and application. *Computer Vision and Image Understanding*, 61(1):38–59, 1995.
- [31] B. N. Cuffin. Eeg localization accuracy improvements using realistically shaped head models. *IEEE Trans. Biomed. Eng.*, 43(3):299–303, 1996.
- [32] A. M. Dale, B. Fischl, and M. I. Sereno. Cortical surface-based analysis i. segmentation and surface reconstruction. *NeuroImage*, 9:179–194, 1999.
- [33] C. Davatzikos. Spatial transformation and registration of brain images using elastically deformable models. *Computer Vision and Image Understanding*, 66(2):207–222, 1997.
- [34] C. Davatzikos and R. N. Bryan. Using a deformable surface model to obtain a shape representation of the cortex. *IEEE Trans. Med. Imag.*, 15(6):785–795, 1996.
- [35] J. C. de Munck. A linear discretization of the volume conductor boundary integral equation using analytically integrated elements. *IEEE Trans. Biomed. Eng.*, 39(9):986–990, 1992.
- [36] P. A. Van den Elsen, J. B. A. Maintz, E-J. D. Pol, and M. A. Viergever. Automatic registration of ct and mr brain images using correlation of geometrical features. *IEEE Trans. Med. Imag.*, 14(2):384–396, 1995.
- [37] R. Deriche. Using canny’s criteria to derive a recursively implemented optimal edge detector. *International Journal of Computer Vision*, 1:167–187, 1987.
- [38] M. Eck and H. Hoppe. Automatic reconstruction of b-spline surfaces of arbitrary topological type. *Computer Graphics*, 30:325–334, 1996.
- [39] H. Edelsbrunner and E. P. Mücke. Three-dimensional alpha shapes. *ACM Trans. on Graphics*, 13(1):43–72, 1994.
- [40] A. Ekoule, F. Peyrin, and R. Goutte. Reconstruction and display of biomedical structures by triangulation of 3d surfaces. *SPIE Science and Engineering of Medical Imaging*, 1137:106–113, 1989.
- [41] A. B. Ekoule, F. C. Peyrin, and C. L. Odet. A triangulation algorithm from arbitrary shaped multiple planar contours. *ACM Trans. on Graphics*, 10(2):182–199, 1991.
- [42] T. L. Faber and E. M. Stokely. Orientation of 3-d structures in medical images. *IEEE Trans. Pattern Anal. Machine Intell.*, 10(5):626–633, 1988.
- [43] J. Feldmar, N. Ayache, and F. Betting. 3d-2d projective registration of free-form curves and surfaces. *Computer Vision and Image Understanding*, 65(3):403–424, 1997.

- [44] M. Fleute and S. Lavallée. Nonrigid 3-d/2-d registration of images using statistical models. In C. Taylor and A. Cochester, editors, *Lecture Notes in Computer Science 1679: Medical Image Computing and Computer-Assisted Intervention, MiCCAI'99*, pages 138–147. Springer, 1999.
- [45] H. Fuchs, Z. M. Kedem, and S. P. Uselton. Optimal surface reconstruction from planar contours. *Communications of the ACM*, 20(10):693–702, 1977.
- [46] S. Ganapathy and T. G. Dennehy. A new general triangulation method for planar contours. *Computer Graphics: A Quarterly Report of SIGGRAPH-ACM*, 16(3):69–74, 1982.
- [47] M. Garreau, J. L. Coatrieux, R. Collorec, and C. Chardenon. A knowledge-based approach for 3-d reconstruction and labeling of vascular networks from biplane angiographic projections. *IEEE Trans. Med. Imag.*, 11(4):517–529, 1992.
- [48] D. Geiger, A. Gupta, L. A. Costa, and J. Vlontzos. Dynamic programming for detecting, tracking and matching deformable contours. *IEEE Trans. Pattern Anal. Machine Intell.*, 17(3):294–302, 1995.
- [49] O. Gérard and S. Makram-Ebeib. Automatic contour detection by encoding knowledge into active contour models. In *IEEE Workshop on Applications of Computer Vision*, 1998.
- [50] N. A. Golias and T. D. Tsiboukis. An approach to refining three-dimensional tetrahedral meshes based on delaunay transformations. *International Journal for Numerical Methods in Engineering*, 37:793–812, 1994.
- [51] A. Guéziec, P. Kazanzides, B. Williamson, and R. H. Taylor. Anatomy-based registration of ct-scan and intraoperative x-ray images for guiding a surgical robot. *IEEE Trans. Med. Imag.*, 17(5):715–728, 1998.
- [52] A. Gupta, T. O'Donnell, and A. Singh. Segmentation and tracking of cine cardia mr and ct images using a 3-d deformable model. In *Proc. IEEE Conf. Computers in Cardiology*, pages 661–664, 1994.
- [53] T. D. Haig, Y. Attikiouzel, and M. Alder. Border marriage: Matching of contours of serial sections. *IEE PROCEEDINGS-I*, 138(5):371–376, 1991.
- [54] M. Hämmäläinen, R. Hari, R. J. Ilmoniemi, J. Knuuttila, and O. V. Lounasmaa. Magnetoencephalography - theory, instrumentation, and applications to noninvasive studies of the working human brain. *Reviews of Modern Physics*, 65(2):413–460, 1993.
- [55] M. Hämmäläinen and J. Nenonen. *Encyclopedia of Electrical Engineering*, volume 12, chapter Magnetic Source Imaging. New Your: Wiley & Sons, 1999.
- [56] A. Hilton, A. J. Stoddart, J. Illingworth, and T. Windeatt. Marching triangles: Range image fusion for complex object modelling. In *IEEE International Conference on Image Processing*, pages 381–384, 1996.
- [57] H. Hoppe, T. DeRose, T. Duchamp, J. McDonald, and W. Stuetzle. Surface reconstruction from unorganized points. *Computer Graphics*, 26(2):71–78, 1992.
- [58] H. Hoppe, T. DeRose, T. Duchamp, J. McDonald, and W. Stuetzle. Mesh optimization. In *Computer Graphics Proceedings, SIGGRAPH*, pages 19–26, 1993.
- [59] R. Hren and G. Stroink. Application of the surface harmonic expansions for modeling the human torso. *IEEE Trans. Biomed. Eng.*, 42(5):521–524, 1995.
- [60] R. Hren, X. Zhang, and G. Stroink. Comparison between electrocardiographic and magnetocardiographic inverse solutions using the boundary element method. *Med. & Biol. Eng. & Comp.*, 34:110–114, 1996.
- [61] A. K. Jain, Y. Zhong, and S. Lakshmanan. Object matching using deformable templates. *IEEE Trans. Pattern Anal. Machine Intell.*, 18(3):267–277, 1996.
- [62] A. E. Johnson and M. Hebert. Control of polygonal mesh resolution for 3-d computer vision. *Graphical Models and Image Processing*, 60(4):261–285, 1998.

- [63] A. D. Kalvin and R. H. Taylor. Surfaces: Polygonal mesh simplification with bounded error. *IEEE Computer Graphics and Applications*, 16(5):64–77, 1996.
- [64] M. Kass, A. Witkin, and D. Terzopoulos. Snakes: Active contour models. *International Journal of Computer Vision*, 1:321–331, 1987.
- [65] N. Kehtarnavaz, L. R. Simar, and R. J. P. de Figueiredo. A syntactic / semantic technique for surface feconstruction from cross-sectional contours. *Computer Vision, Graphics and Image Processing*, 42:399–409, 1988.
- [66] E. Keppel. Approximating complex surfaces by triangulation of contour lines. *IBM Journal of Research, Development*, 19(1):2–11, 1975.
- [67] Y. Kim and R. C. Luo. Surface reconstruction based on descriptions of cross-sectional contours. *SPIE Sensing and Reconstruction of Three-Dimensional Objects and Scenes*, 1260:191–198, 1990.
- [68] S. Kumar, S. Han D. Goldgof, and K. Bowyer. On recovering hyperquadrics from range data. *IEEE Trans. Pattern Anal. Machine Intell.*, 17(11):1079–1083, 1995.
- [69] J-O. Lachaud and A. Montanvert. Deformable meshes with automated topology changes for coarse-to-fine three-dimensional surface extraction. *Med. Image Anal.*, 3(2):187–207, 1999.
- [70] S. Lavallée and R. Szeliski. Recovering the position and orientation of free-form objects from image contours using 3d distance maps. *IEEE Trans. Pattern Anal. Machine Intell.*, 17(4):378–390, 1995.
- [71] B. Lelieveldt. *Anatomical Models in Cardiovascular Image Analysis*. PhD thesis, University of Leiden, the Netherlands, 1999.
- [72] W.E. Lorensen and H. E. Cline. Marching cubes: A high resolution 3d surface construction algorithm. *Computer Graphics*, 21:163–169, 1987.
- [73] J. Lötjönen, O. Sipilä, J. Nenonen, K. Lauerma, T. Jokiniemi, P-J. Reissman, H. Pohjonen, and T. Katila. Individual boundary element models for magnetocardiographic applications. In *International Conference of IEEE Engineering in Medicine and Biology Society*, pages CD-ROM, 1996.
- [74] F. Maes, A. Collignon, D. Vandermeulen, G. Marchal, and P. Suetens. Multimodality image registration by maximization of mutual information. *IEEE Trans. Med. Imag.*, 16(2):187–198, 1997.
- [75] J. B. A. Maintz and M. A. Viergever. A survey of medical image registration. *Med. Image Anal.*, 2(1):1–36, 1998.
- [76] R. Malladi, J. A. Sethian, and B. C. Vemuri. Shape modeling with front propagation: A level set approach. *IEEE Trans. Pattern Anal. Machine Intell.*, 17(2):158–175, 1995.
- [77] W. N. Martin and J. K. Aggarwal. Volumetric descriptions of objects from multiple views. *IEEE Trans. Pattern Anal. Machine Intell.*, 5(2):150–158, 1983.
- [78] C. R. Maurer, B. Aboutanos, B. M. Dawant, R. J. Maciunas, and J. M. Fitzparick. Registration of 3-d images using weighted geometrical features. *IEEE Trans. Med. Imag.*, 15(6):836–849, 1996.
- [79] T. McInerney and R. Kikinis. An object-based volumetric deformable atlas for the improved localization of neuroanatomy in mr images. In W. M. Wells, A. Colchester, and S. Delp, editors, *Lecture Notes in Computer Science 1496: Medical Image Computing and Computer-Assisted Intervention, MICCAI98*, pages 861–869. Springer, 1998.
- [80] T. McInerney and D. Terzopoulos. Deformable models in medical image analysis: a survey. *Med. Image Anal.*, 1(2):91–108, 1996.
- [81] J. V. Miller, D. E. Breen, W. E. Lorensen, R. M O’Bara, and M. J. Wozny. Geometrically deformed models: A method for extracting closed geometric models from volume data. *Computer Graphics*, 25(4):217–226, 1991.

- [82] F. Morady. Radio-frequency ablation as treatment for cardiac arrhythmias. *The New England Journal of Medicine*, 340(7):534–544, 1999.
- [83] J. Nenonen and T. Katila. Noninvasive functional localization by biomagnetic methods. *Journal of Clinical Engineering*, 16(5):423–434, 1991.
- [84] J. Nenonen, J. Montonen, and M. Mäkijärvi. Principles of magnetocardiographic mapping. In M. Shensea, M. Borgreffe, and G. Breithardt, editors, *Cardiac Mapping*. Mount Kisco, NY: Futura Publishing Co, in press.
- [85] J. Nenonen, K. Pesola, J. Lötjönen, K. Lauerma, H. Hänninen, P. Korhonen, M. Mäkijärvi, R. Fenici, and T. Katila. Cardiomagnetic source imaging studies with focal and distributed source models. *Biomedizinische Technik*, 44(suppl. 2):135–138, 1999.
- [86] T. O'Donnell, X-S. Fang, T. E. Boulton, and A. Gupta. The extruded generalized cylinder: A deformable model for object recovery. In *Proc. IEEE Computer Vision and Pattern Recognition Conf.*, pages 174–180, 1994.
- [87] K. M. Oh and K. H. Park. A vertex merging algorithm for extracting a variable-resolution isosurface from volume data. In *IEEE International Conference on Systems, Man and Cybernetics*, pages 3543–3548, 1995.
- [88] C. A. Pelizzari, G. T. Y. Chen, D. R. Spelbring, R. R. Weichselbaum, and C-T. Chen. Accurate three-dimensional registration of ct, pet, and/or mr images of the brain. *Journal of Computer Assisted Tomography*, 13(1):20–26, 1989.
- [89] A. Pentland and B. Horowitz. Recovery of nonrigid motion and structure. *IEEE Trans. Pattern Anal. Machine Intell.*, 13(7):730–742, 1991.
- [90] A. Pentland and S. Sclaroff. Closed-form solutions for physically based shape modeling and recognition. *IEEE Trans. Pattern Anal. Machine Intell.*, 13(7):715–729, 1991.
- [91] K. Pesola, J. Nenonen, R. Fenici, J. Lötjönen, M. Mäkijärvi, P. Fenici, P. Korhonen, K. Lauerma, M. Valkonen, L. Toivonen, and T. Katila. Bio-electromagnetic localization of a pacing catheter in the heart. *Phys. Med. Biol.*, 44:2565–2578, 1999.
- [92] M. Pietikäinen. *Detection of knots in Logs using X-ray Imaging*. PhD thesis, University of Oulu, 1996.
- [93] H. Pohjonen, P. Nikkinen, O. Sipilä, J. Launes, E. Salli, O. Salonen, P. Karp, J. Ylä-Jääski, T. Katila, and K. Liewendahl. Registration and display of brain spect and mri using external markers. *Neuroradiology*, 38:108–114, 1996.
- [94] S. Sandor and R. Leahy. Surface-based labeling of cortical anatomy using a deformable atlas. *IEEE Trans. Med. Imag.*, 16(1):41–54, 1997.
- [95] W. J. Schroeder, J. A. Zarge, and W. E. Lorensen. Decimation of triangle meshes. *Computer Graphics*, 26(2):65–70, 1992.
- [96] L. L. Schumaker. Reconstruction of 3d objects using splines. In *SPIE Vol. 1990 Curves and Surfaces in Computer Vision and Graphics*, pages 130–140, 1990.
- [97] T. W. Sederberg and S. Parry. Free-form deformation of solid geometric models. *Computer Graphics, SIGGRAPH*, 20(4):151–160, 1986.
- [98] M. Shantz. Surface definition for branching, contour-defined objects. *Computer Graphics: A Quarterly Report of SIGGRAPH-ACM*, 15(2):242–269, 1981.
- [99] D. N. Shenton and Z. J. Cendes. Three-dimensional finite element mesh generation using delaunay tessellation. *IEEE Trans. Magn.*, 21(6):2535–2538, 1985.
- [100] A. Singh, D. Goldgof, and D. Terzopoulos. *Deformable Models in Medical Image Analysis*. IEEE Computer Society Press, 1998.
- [101] M. Soucy and D. Laurendeau. Multiresolution surface modeling based on hierarchical triangulation. *Computer Vision and Image Understanding*, 63(1):1–14, 1996.

- [102] L. H. Staib and J. S. Duncan. Boundary finding with parametrically deformable models. *IEEE Trans. Pattern Anal. Machine Intell.*, 14(11):1061–1075, 1992.
- [103] L. H. Staib and J. S. Duncan. Model-based deformable surface finding for medical images. *IEEE Trans. Med. Imag.*, 15(5):720–731, 1996.
- [104] G. Stroink, R. Lamothe, and M. J. Gardner. Magnetocardiographic and electrocardiographic mapping studi. In H. Weinstock, editor, *SQUID Sensors: Fundamentals, Fabrication and Applications*, pages 413–444. Kluwer: NATO ASI Series, 1996.
- [105] G. Stroink, W. Moshage, and S. Achenback. Cardiomagnetism. In W. Andrä and H. Nowak, editors, *Magnetism in Medicine*, pages 136–189. Berlin: Wiley-VCH, 1998.
- [106] Y. Sun, I. Liu, and J. K. Grady. Reconstruction of 3-d binary tree-like structures from three mutually orthogonal projections. *IEEE Trans. Pattern Anal. and Machine Intell.*, 16(3):241–248, 1994.
- [107] G. Székely, A. Kelemen, C. Brechbühler, and G. Gerig. Segmentation of 2-d and 3-d objects from mri volume data using constrained elastic deformabtions of flexible fourier contour and surface models. *Med. Image Anal.*, 1(1):19–34, 1996.
- [108] R. Szeliski and S. Lavallée. Matching 3-d anatomical surfaces with non-rigid deformations using octree-splines. *International Journal of Computer Vision*, 18:1–18, 1996.
- [109] D. Terzopoulos and D. Metaxas. Dynamic 3d models with local and global deformations: Deformable superquadrics. *IEEE Trans. Pattern Anal. Machine Intell.*, 13(7):703–714, 1991.
- [110] D. Terzopoulos, A. Witkin, and M. Kass. Constraints on deformable models: Recovering 3d shape and nonrigid motion. *Artificial Intelligence*, 36:91–123, 1988.
- [111] R. D. Throne and L. G. Olson. The effects of errors in assumed conductivities and geometry on numerical solutions to the inverse problem of electrocardiography. *IEEE Trans. Biomed. Eng.*, 42(12):1192–1200, 1995.
- [112] L. Van Tran, R. C. Bahn, and J. Sklansky. Reconstructing the cross sections of coronary arteries from biplane angiograms. *IEEE Trans. Med. Imag.*, 11(4):517–528, 1992.
- [113] L. Traversoni. Delaunay’s tetrahedralization; an efficient algorithm for 3d triangulation. In *SPIE Vol. 1251 Curves and Surfaces in Computer Vision and Graphics*, pages 56–61, 1990.
- [114] G. Turk. Re-tiling polygonal surfaces. *Computer Graphics*, 26(2):55–64, 1992.
- [115] A. van Oosterom, T. F. Oostendorp, G. J. Huiskamp, and H. J. M. ter Brake. The magneto-cardiogram as derived from electrocardiographic data. *Circulation Research*, 67(6):1503–1509, 1990.
- [116] R. C. Veltkamp. Boundaries through scattered points of unknown density. *Graphical Models and Image Processing*, 57(6):441–452, 1995.
- [117] A. Wahle, H. Oswald, and E. Fleck. 3d heart-vessel reconstruction from biplane angiograms. *IEEE Computer Graphics and Applications*, 16(1):65–73, 1996.
- [118] D. F. Watson. Computing the n-dimensional delaunay tessellation with application to voronoi polytopes. *The Computer Journal*, 24(2):167–172, 1981.
- [119] N. P. Weatherill and O. Hassan. Efficient three-dimensional delaunay triangulation with automatic point creation and imposed boundary constraints. *International Journal for Numerical Methods in Engineering*, 37:2005–2039, 1994.
- [120] R. P. Woods, J. C. Mazziotta, and S. R. Cherry. Mri-pet registration with automated algorithm. *Journal of Computer Assisted Tomography*, 17(4):536–546, 1993.
- [121] J. P. Wright and A. G. Jack. Aspects of three-dimensional constrained delaunay meshing. *International Journal for Numerical Methods in Engineering*, 37:1841–1861, 1994.
- [122] C. Xu, D. L. Pham, M. E. Rettmann, D. N. Yu, and J. L. Prince. Reconstruction of the human cerebral cortex from magnetic resonance images. *IEEE Trans. Med. Imag.*, 18(6):467–480, 1999.

- [123] C. Xu and J. L. Prince. Snakes, shapes, and gradient vector flow. *IEEE Trans. Image Proc.*, 7(3):359–369, 1998.
- [124] B. Yvert, O. Bertrand, J. F. Echallier, and J. Pernier. Improved forward eeg calculations using local mesh refinement of realistic head geometries. *Electroencephalography and clinical Neurophysiology*, 95:381–392, 1995.
- [125] B. Yvert, O. Bertrand, J. F. Echallier, and J. Pernier. Improved dipole localization using local mesh refinement of realistic head geometries: an eeg simulation study. *Electroencephalography and clinical Neurophysiology*, 99:79–89, 1996.
- [126] J. M. Zhou, K. D. Zhou, and K. R. Shao. Automatic generation of 3d meshes for complicated solids. *IEEE Trans. Magn.*, 28(2):1759–1762, 1992.
- [127] M. J. Zyda, A. R. Jones, and P. G. Hogan. Surface construction from planar contours. *Computer & Graphics*, 11(4):393–408, 1987.